

BEACON: JWST NIRCam Pure-parallel Imaging Survey. IV.

A Systematic Search for Galaxy Overdensities and Evidence for Gas Accretion Mode Transition

RYO ALBERT SUTANTO ,¹ TAKAHIRO MORISHITA ,^{2,1} TADAYUKI KODAMA ,¹ ABDURRO'UF ,³ LARRY D. BRADLEY ,⁴ ANDREW J. BUNKER ,⁵ NIMA CHARTAB ,² NUO CHEN ,¹ MATTHEW J. HAYES ,⁶ GEORGE HELOU ,² NOVAN SAPUTRA HARYANA ,¹ NICHA LEETHOCHAWALIT ,⁷ ZHAORAN LIU ,^{1,8} CHARLOTTE A. MASON ,^{9,10} MARC RAFELSKI ,^{4,11} MICHAEL J. RUTKOWSKI ,¹² MASSIMO STIAVELLI ,⁴ KOSUKE TAKAHASHI ,¹ HARRY I. TEPLITZ ,² MICHELE TRENTI ,¹³ TOMMASO TREU ,¹⁴ BENEDETTA VULCANI ,¹⁵ AND YECHI ZHANG ,²

¹ *Astronomical Institute, Tohoku University, 6-3 Aramaki, Aoba-ku, Sendai 980-8578, Japan*

² *IPAC, California Institute of Technology, MC 314-6, 1200 E. California Boulevard, Pasadena, CA 91125, USA*

³ *Department of Astronomy, Indiana University, 727 East Third Street, Bloomington, IN 47405, USA*

⁴ *Space Telescope Science Institute, 3700 San Martin Drive, Baltimore, MD 21218, USA*

⁵ *Department of Physics, University of Oxford, Denys Wilkinson Building, Keble Road, Oxford OX1 3RH, UK*

⁶ *Stockholm University, Department of Astronomy and Oskar Klein Centre for Cosmoparticle Physics, AlbaNova University Centre, SE-10691, Stockholm, Sweden*

⁷ *National Astronomical Research Institute of Thailand (NARIT), Mae Rim, Chiang Mai, 50180, Thailand*

⁸ *MIT Kavli Institute for Astrophysics and Space Research, 70 Vassar Street, Cambridge, MA 02139, USA*

⁹ *Cosmic Dawn Center (DAWN), Denmark*

¹⁰ *Niels Bohr Institute, University of Copenhagen, Jagtvej 128, DK-2200 Copenhagen N, Denmark*

¹¹ *Department of Physics and Astronomy, Johns Hopkins University, Baltimore, MD 21218, USA*

¹² *Minnesota State University, Mankato, Department of Physics and Astronomy, 141 Trafton Science Center N, Mankato, MN 56001, USA*

¹³ *School of Physics, The University of Melbourne, VIC 3010, Australia*

¹⁴ *Department of Physics and Astronomy, University of California, Los Angeles, 430 Portola Plaza, Los Angeles, CA 90095, USA*

¹⁵ *INAF – Osservatorio Astronomico di Padova, Vicolo Osservatorio 5, 35122 Padova, Italy*

ABSTRACT

We systematically search for galaxy overdensities using 20 independent fields with a minimum of six filters (F090W, F115W, F150W, F277W, F356W, and F444W) from BEACON, the JWST Cycle 2 NIRCam pure-parallel imaging survey. We apply an adaptive kernel-density estimation method that incorporates the full photometric redshift probability distribution function of each galaxy to map galaxy overdensities, and identify 207 significant ($> 4\sigma$) overdensities at $1.5 < z < 5$. We measure the quenched-galaxy fraction, the median specific star formation rate (sSFR), the total halo mass, and the local galaxy density of each system. By investigating the correlation among these observables, we find that galaxy quenching proceeds in two paths: (i) Overdensities within more massive halos exhibit higher quenched fractions and lower averaged sSFRs. This trend weakens at $z \gtrsim 2$, consistent with cold gas streams penetrating shock-heated massive halos and sustaining star formation activity at early times. (ii) We also find a dependence of the same parameters on local densities at $z < 2$, where the quenched fraction increases and the sSFR decreases toward higher densities. The environmental trend in sSFR weakens at $z \sim 2\text{--}3$ and shows tentative evidence for a reversal at $z > 3$, potentially due to a larger cold gas supply in earlier times. Our study reveals a complex interplay between individual galaxies and large-scale environmental properties, marking the onset of environmental effects on galaxy quenching in massive halos at cosmic noon.

Keywords: Galaxies (323) — Galaxy evolution (594) — High-redshift galaxies (734) — Protocluster (1297) — Galaxy environments (2029)

1. INTRODUCTION

Email: ryo.sutanto@astr.tohoku.ac.jp

The structure growth in our universe originates from fluctuations in the dark matter distributions, which lead

to the formation of stars and galaxies through the interplay of gravitational collapse and hydrodynamical processes (S. D. M. White & C. S. Frenk 1991; S. Cole et al. 2000; V. Springel et al. 2005). The availability and regulation of gas in these systems play crucial roles in shaping their physical properties. Dense environments at high redshifts, especially along cosmic filaments and their cores, provide unique conditions through the supply of cold gas at an accelerated pace, resulting in the enhancement of early galaxy growth.

Some of the earliest evidence for environmental effects on galaxy evolution was observed among galaxy members in local clusters (H. Butcher & A. Oemler Jr 1978; A. Dressler 1980). These studies revealed clear differences in galaxy colors and morphologies compared to their field counterparts, indicating the influence of dense environments on galaxy evolution. Local clusters are dense and dynamically hot, which can affect the galaxies therein through several processes, such as strangulation/starvation (R. B. Larson et al. 1980), ram-pressure stripping (J. E. Gunn & J. R. Gott III 1972; M. G. Abadi et al. 1999), and tidal stripping (B. Moore et al. 1996, 1998).

These environmental effects are expected to differ at higher redshifts, where most galaxy systems are still young and not yet virialized (A. J. Davis et al. 2011; S. I. Muldrew et al. 2015). This evolutionary stage, commonly referred to as the *protocluster* phase, precedes the formation of a hot intracluster medium, which is thought to be responsible for several of the environmental processes observed in mature clusters mentioned above. Recent studies have extended such investigations to higher redshifts ($2 < z < 6$) and found evidence of environmental effects in some systems, seen as an enhancement of quiescent galaxies (A. Naufal et al. 2024; J. M. Pérez-Martínez et al. 2025; T. Morishita et al. 2025a) and an offset in the mass-metallicity relation (R. Shimakawa et al. 2015).

A common approach to studying environmental effects is to relate galaxy properties directly to their local environments, rather than solely to the scale of the host systems (i.e., halo masses or size). This requires quantifying the environment using spatial information on the two-dimensional sky plane together with redshift. Several methods have been commonly used to characterize galaxy environments, including fixed apertures, nearest-neighbor (k-NN) estimators, Voronoi tessellation, weighted kernel density estimation (wKDE), and more advanced approaches such as AMICO and PZWav (see B. Darvish et al. 2015 and R. Adam et al. 2019 for reviews of these methods).

Studies using these approaches have shown that galaxy properties exhibit significant correlations with the environment up to $z \sim 2$, with higher density regions hosting galaxies that, on average, have lower star formation rate (SFR) and specific star formation rate (sSFR), but higher stellar mass (M_*) (B. Darvish et al. 2016; N. Chartab et al. 2020; K. Shi et al. 2024; S. Taamoli et al. 2024; H. Hatamnia et al. 2025; Z. Liu et al. 2025). Interestingly, some studies have reported a reversal of these trends, particularly in SFR and sSFR, around $z \sim 1$ (D. Elbaz et al. 2007; M. C. Cooper et al. 2008), while more recent studies have suggested that this transition may occur at even higher redshifts ($z > 2$; B. Lemaux et al. 2022; S. Taamoli et al. 2024). This effect may be attributed to the higher rates of merger events or more efficient gas supply during this epoch. However, this observed behavior could be affected by cosmic variance or selection effects, hampering us from obtaining a robust consensus. Recent work modeling selection effects in environmental studies shows that an sSFR-environment reversal is not expected at $z \sim 2 - 3$, and if present, occurs at $z > 3$ (N. Chartab et al. 2025).

In addition, physically interpreting this reversal effect requires a framework describing how gas regulation changes across cosmic time and halo mass. Numerical simulations by A. Dekel & Y. Birnboim (2006) suggest that gas accretion is linked to halo mass, dividing the accretion mode into three regimes: cold, hot, and cold in hot. At low redshifts, massive systems exhibit shock-heated halos that can efficiently heat incoming cold gas, preventing new star formation. However, at high redshift ($z > 2$), gas accretion can remain cold through dense filamentary streams (A. Dekel et al. 2009). The transition epoch of this accretion mode—when cold-mode accretion begins to shut off and hot-mode accretion becomes dominant, corresponds to the “cosmic noon”, the period during which the comoving cosmic star formation rate density reaches its peak (P. Madau & M. Dickinson 2014).

Several observational studies support this scenario. For example, the ratios of Ly α luminosity and star formation rate (SFR) to the expected baryon accretion rate (BAR) show a clear flattening above the cold-stream threshold, while exhibiting a scaling relation in the hot-accretion regime. (E. Daddi et al. 2022a; N. B. Sillassen et al. 2024). Wide-field dual narrow-band imaging observations of Ly α and H α emitters in and around young protoclusters at $z = 2 - 2.5$ have revealed the physical association of HI gas in dense environments such as cores and surrounding filaments probably fed by cold-mode accretions, as indicated by poor visibility of Ly α emitters with respect to H α emitters in those dense environments.

vironments (R. Shimakawa et al. 2017; K. Daikuhara et al. 2025, M. Funaki et al. 2026, in preparation). Other studies also point to a transition from the metal-deficient to metal-rich systems around $z \sim 2$, compared to field galaxies, as evidence for a change in gas accretion mode (N. Chartab et al. 2021; J. M. Pérez-Martínez et al. 2024; K. Adachi et al. 2025).

Although significant progress has been made, studies of galaxy environments at high redshift are often limited to contiguous survey fields, raising concerns that some reported trends may be influenced by cosmic variance (e.g., M. Trenti & M. Stiavelli 2008). This limitation complicates the interpretation of environmental effects and their connection to the underlying physical processes. The pure-parallel imaging mode, enabled for HST (M. Trenti et al. 2012; L. Bradley et al. 2012; K. B. Schmidt et al. 2014; T. Morishita et al. 2018, 2020) and now for JWST (C. C. Williams et al. 2025; T. Morishita et al. 2025b), provides several key advantages for overcoming these limitations by observing many independent pointings distributed across the sky with exquisite sensitivity. The pure-parallel imaging strategy substantially reduces the impact of cosmic variance, while the depth of JWST NIRCam observations enables the detection of lower-mass galaxies out to higher redshift compared to that of HST. In addition, the multi-band coverage of the survey yields high-quality photometric redshift measurements, which are well suited for constraining galaxy clustering. Together, these characteristics make the mode an ideal approach to a systematic and unbiased search for galaxy overdensities and to investigating how galaxy properties depend on both halo mass and local environment at high redshift.

In this paper, we perform a search for galaxy overdensities at $1.5 < z < 7$ in 20 NIRCam pointings observed in the JWST Cycle 2 pure-parallel NIRCam imaging survey, Bias-free Extragalactic Analysis for Cosmic Origins with NIRCam (BEACON; T. Morishita et al. 2025b, Y. Zhang et al. 2026, K. Kreilgaard, in prep.). Our study adopts the weighted-adaptive kernel density estimation (wKDE) method to fully utilize our photometric redshift probability distribution function. This paper is organized as follows. In Section 2, we summarize the BEACON observations, parameter estimations, and the construction of our final galaxy sample for the overdensity search. Section 3 introduces the weighted-adaptive KDE method. In Section 4, we outline the criteria used to define the final catalog of galaxy overdensities, present the results of our overdensity search, and highlight several prominent systems from the catalog. We also describe the procedures used to estimate the physical properties of the identified systems. In Section 5,

we discuss the properties of galaxies both on the system scale, which links to total halo mass, and on the local scale, which links to the overdensity factor. Finally, we summarize our findings in Section 6.

Throughout this paper, we adopt the standard cosmology model Λ CDM with $\Omega_m = 0.3$, $\Omega_\Lambda = 0.7$, and $H_0 = 70 \text{ km s}^{-1} \text{ Mpc}^{-1}$. Photometric measurements are reported in the AB magnitude system (J. B. Oke & J. E. Gunn 1983; M. Fukugita et al. 1995).

2. DATA AND SAMPLE

2.1. *Observation*

We use the JWST photometric datasets from the Cycle 2 NIRCam pure-parallel imaging program, BEACON (GO-3990; PI: T. Morishita; Co-PIs: C. Mason, T. Treu, M. Trenti; T. Morishita et al. 2025b). The configuration of this survey follows a parallel observing mode, in which multiple JWST science instruments operate simultaneously, with one serving as the primary instrument and others as parallel instruments observing different regions of the focal plane. Therefore, the configuration of the parallel observation on each visit to the field is different, particularly the exposure times and filter configurations. To ensure the uniformity of our analysis and high accuracy on the photometric redshift, we select the 20 fields from the full BEACON DR2 (K.C. Kreilgaard, in prep.) with a requirement of a minimum of 6 filters, with the shortest filter F090W and the longest filter either F444W/F480M. This ensures that we trace the Balmer break features at $z = 1.5 - 7$. From this collection of fields, we have a total area of $\sim 400 \text{ arcmin}^2$ and achieve 10σ limiting depths in the F444W band of $m_{\text{F444W}} \approx 27.3 - 28.6$ across the field.

The detail of the photometry extraction for our data is detailed in T. Morishita et al. (2025b), and we briefly summarize the procedure here. Sources were identified by their detection image, which is the rms-weighted combination of F277W + F356W + F444W, using SOURCEEXTRACTOR (E. Bertin & S. Arnouts 1996). We adopt the aperture flux with $0.^{\prime\prime}16$ radius on the PSF-matched image on F444W, scaled by $f_{\text{auto}, \text{F444W}}/f_{\text{aper}, \text{F444W}}$ to maintain the colors while using total fluxes for deriving galaxy parameters. All of the measured fluxes are corrected for the galactic dust reddening value at the corresponding field location taken from the NASA/IPAC Extragalactic Database (D. J. Schlegel et al. 1998; E. F. Schlafly & D. P. Finkbeiner 2011). We use the reddening curve of Milky Way dust law (J. A. Cardelli et al. 1989).

2.2. Photometric Redshift

We create a photometric redshift catalog utilizing EAZY-PY (G. B. Brammer et al. 2008), which provides us direct measurement for the zero-point corrections for each catalog. Photometric redshift fitting is performed using the EAZY software by fitting linear combination templates to the data using chi-square minimization. In contrast to previous BEACON studies, we carry out our own photometric redshift SED fitting to obtain the complete photometric redshift probability distribution function (PDF). We choose the template library `tweak_fspS_QSF_12_v3.param`, which consists of 12 templates derived from the flexible stellar population synthesis model (FSPS) code (C. Conroy et al. 2010) and offers the lowest outlier fraction. We set the redshift range to $0 < z < 12$, with $0.01(1+z)$ increment. We use the magnitude prior provided by EAZY, `prior_F160W_TAO.dat`, using F444W.

To account for the uncertainties of the photometric redshift, we use its full probability distribution function, $P(z)$, for our main analysis below. Using the complete PDF of the redshift, we can define multiple redshift values, such as z_{peak} , which represents the redshift with the highest probability in the PDF, and z_{50} , which represents the median-posterior redshift and is more representative of the PDF's central tendency. Throughout this paper, when defining a representative redshift value beyond its PDF, we use z_{50} .

We assess the accuracy of the photometric redshift by cross-matching the galaxy sample from the BEACON fields located in regions overlapping with one of four legacy fields (COSMOS, EGS, GOODS-S, and UDS), where a spectroscopic redshift catalog from various surveys is available, that is, 3DHST (G. B. Brammer et al. 2012; R. E. Skelton et al. 2014), COSMOS (A. A. Khostovan et al. 2025), GOODS/FORS2 (E. Vanzella et al. 2008), GOODS/VIMOS (I. Balestra et al. 2010), VANDELS (B. Garilli et al. 2021), CANDELS/HLSP (N. A. Grogin et al. 2011; A. M. Koekemoer et al. 2011), GOODS/JADES (A. J. Bunker et al. 2024; F. D'Eugenio et al. 2025; E. Curtis-Lake et al. 2025), and CEERS (S. L. Finkelstein et al. 2023). The comparison of our photometric redshift with the spectroscopic redshift is presented in Figure 1. We calculate the median absolute deviation of our photometric redshift fitting by using

$$\sigma_{\text{NMAD}} = 1.48 \times \text{median} \left(\left| \frac{\Delta z - \text{median}(\Delta z)}{1 + z_{\text{spec}}} \right| \right) \quad (1)$$

with $\Delta z = z_{\text{phot}} - z_{\text{spec}}$. From this measurement, we get $\sigma_{\text{NMAD}} = 0.024$, with the number of outliers, defined by $\Delta z/(1+z) > 5\sigma$, reaching below 10% for galaxies at $z_{\text{phot}} > 1.5$. This assures that the photometric measure-

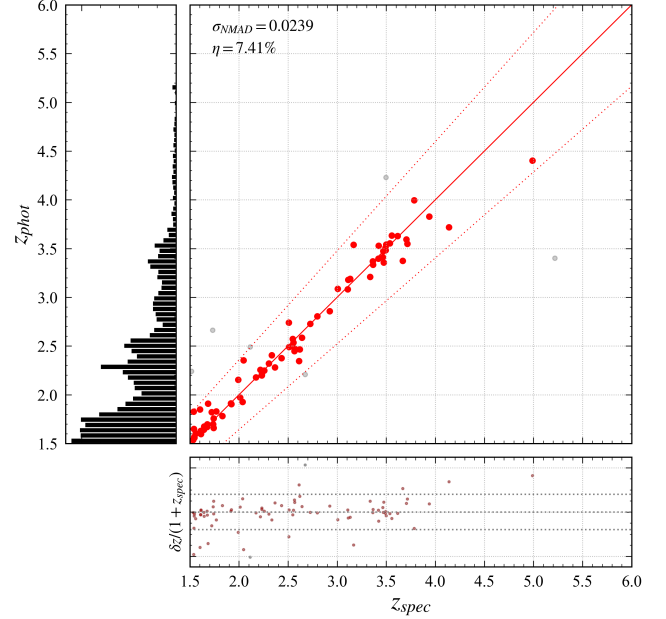


Figure 1. Comparison between EAZY-derived photometric redshifts and spectroscopic redshifts compiled from various previous studies. Red dotted line corresponds to the outlier limit between photometric redshift and spectroscopic redshift. Grey dots correspond to the outliers.

ments of our sample are robust enough to perform an analysis for searching overdensity.

2.3. Spectral Energy Distribution Fitting

We derive the basic physical parameters of galaxies through a photometric SED fitting analysis using CIGALE (Code Investigating GALaxy Emission; M. Boquien et al. 2019). All available broad-band filters are used for each field, with a minimum of six filters common to all fields (F090W, F115W, F150W, F277W, F356W, and F444W). Throughout the fitting process, we fixed the redshift to the median photometric redshift value, z_{50} , for each galaxy.

We adopt a delayed exponentially declining star formation history (SFH) model of the form

$$\text{SFR}(t) \propto \frac{t}{\tau^2} \exp \left(-\frac{t}{\tau} \right), \quad (2)$$

where the onset age of star formation, t_0 , ranges from $10^{7.6}$ to $10^{10.1}$ years, and the characteristic timescale, τ , ranges from 10 Myr to 10 Gyr.

The fitting assumes a G. Chabrier (2003) initial mass function (IMF) and employs simple stellar population (SSP) templates from G. Bruzual & S. Charlot (2003). The stellar metallicity is varied over the range $Z = 0.0001\text{--}0.05$, motivated by S. Bellstedt & A. S. Robotham (2025), for which this choice yields stellar masses and star formation rates with minimal bias.

Nebular emission from A. K. Inoue (2011), which was generated using CLOUDY (G. Ferland et al. 1998; G. J. Ferland et al. 2013), is included using templates with an ionization parameter of $\log U = -2.0$. For dust attenuation, we adopt the modified D. Calzetti et al. (2000) law with a nebular color excess of $E(B - V) = 0.0\text{--}1.5$ and a total-to-selective extinction ratio of $R_V = 4.05$. Rest-frame $U - V$ and $V - J$ colors are also computed to be used for classifying galaxies as quiescent or star-forming using UVJ diagram.

Note that we verified that the derived parameters for the main sample remain consistent within the uncertainties when using either z_{50} or the peak redshift z_{peak} , indicating that our results are robust against the choice of redshift estimator.

2.4. Quiescent and Star-forming Galaxies

To investigate the environmental impact on the galaxy quenching process, we classify a population of quiescent galaxies. We select the population of quiescent galaxies utilizing the modified rest-frame UVJ classification from K. E. Whitaker et al. (2012) following K. E. Whitaker et al. (2015), which is defined as

$$\begin{aligned} U - V &> 0.8(V - J) + 0.7 \\ U - V &> 1.3 \end{aligned}$$

We note that the vertical cut of the UVJ selection is not applied here. By doing so, we allow the inclusion of dusty and quiescent galaxies that would have been excluded by the vertical cut (A. van der Wel et al. 2014).

Additionally, we consider an alternative separation of quiescent and star-forming galaxies based on a specific star formation rate (sSFR) cut following A. Carnall et al. (2023), defined as $\text{sSFR} < 0.2/t_H$, where t_H is the age of the Universe at the corresponding redshift. We confirm that the choice of quiescent galaxy selection criterion does not affect the final interpretation of this paper. Therefore, we adopt the UVJ selection throughout our analysis.

2.5. Galaxy Sample

We select our galaxy sample on every field based on the data reduction and photometric measurement criteria:

1. To minimize stellar contamination in our galaxy sample, we exclude objects with `CLASS_STAR` > 0.90 from the `SExtractor` output.
2. Due to different coverage for the short and long channels (caused by the detector chip gaps in the short channel imaging), we only use galaxies covered by the full filter set. For this, we use

`SExtractor` flags, which indicate the photometry of the object to be not truncated or located near the edge of mosaic, `FLAG_SW` < 8, and `FLAG_LW` < 8.

3. To maintain uniformity across all the fields, we cut the magnitude of galaxies by the shallowest field magnitude limit, $m_{\text{F444W,lim}} < 27.3$ ABmag.

In addition, we include constraints from photometric redshift and SED fitting measurements:

1. Quality of fit (reduced χ^2) for the photometric redshift from the `eazy` output in $0.01 < \chi^2_\nu < 5$.
2. Photometric redshift (z_{50}) range in $1.25 < z_{50} < 8$.
3. Photometric redshift error, $\Delta z/(1+z) < 0.4$.
4. Total integrated photometric redshift PDF at $\Delta z \pm 0.5$, $\int_{z_{\text{phot}}-0.5}^{z_{\text{phot}}+0.5} P(z)dz > 0.7$, to constrain the redshift PDF mostly located near the photometric redshift value.

From our 20 fields, we find 8287 galaxies that satisfy all of the above criteria.

2.6. Mass Completeness

The clustering of galaxies is known to depend on their stellar mass, where more massive galaxies are more clustered compared to lower mass galaxies. This trend has been demonstrated in previous studies at redshifts below $z \sim 2$ (B. Meneux et al. 2008; D. A. Wake et al. 2011; R. M. Bielby et al. 2014). This relationship has also been observed to persist at higher redshifts (A. Durkalec et al. 2018; Y. Qiu et al. 2018; Y. Harikane et al. 2018). Therefore, it is important to consider the stellar mass distribution of our sample before searching for overdensities. In this study, we estimate the stellar mass completeness limit of our sample to assess whether a mass cut should be applied.

The stellar mass completeness limit is determined following the method described by L. Pozzetti et al. (2010). We aim to estimate the minimum stellar mass that can be reliably detected based on the magnitude limit we have defined in the previous section. For each galaxy in our sample, we compute its limiting stellar mass ($M_{\text{lim},i}$) by scaling its derived stellar mass (M_i) to our magnitude limit:

$$\log(M_{\text{lim},i}) = \log(M_i) + 0.4(m_{\text{F444W}} - m_{\text{F444W,lim}}). \quad (3)$$

This calculation is performed within redshift bins of width $\Delta z = 0.7$. In each bin, we select the 20% faintest galaxies. We then calculate the 90% percentile of their $M_{\text{lim},i}$ distribution, which adopted as the stellar mass completeness limit (M_{lim}). This definition corresponds to the stellar mass above which the sample is expected to be 90% complete at a given redshift.

The derived mass completeness limit is shown in Figure 2. However, due to relatively small sample size, the

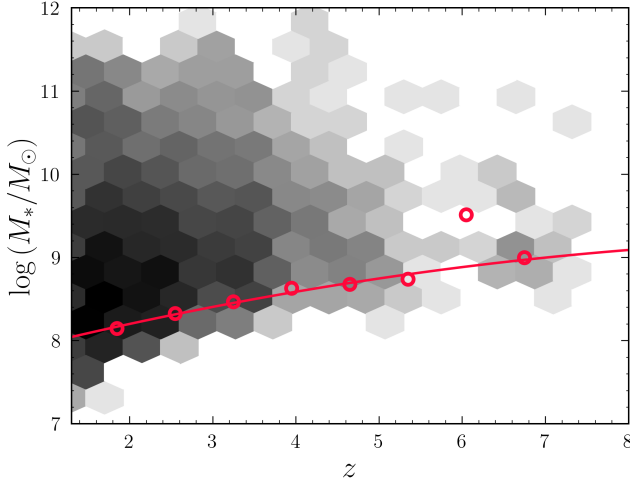


Figure 2. Mass completeness limit for the 20 selected BEACON fields. The 2D hexagon bins show the stellar mass distributions at $0 < z < 8$. Red open circles show the mass completeness limits calculated in the redshift bins with a step of 0.7, with the red line indicating its quadratic fitted function.

completeness estimate at $z \sim 6$ resulted as an outlier. To mitigate this effect, we determine the stellar mass completeness limit as a function of redshift by interpolating the measurements using a quadratic fit.

Using this approach, we find that the stellar mass completeness limit increases from $\log(M_*/M_\odot) = 8.05$ at $z \sim 1.5$ to $\log(M_*/M_\odot) = 8.99$ at $z \sim 7$. Based on these results, we adopt a conservative stellar mass cut of $\log(M_*/M_\odot) = 9.0$ for the analysis presented below. However, we note that no stellar mass cut is applied, on top of the already applied magnitude cut, when constructing the overdensity maps (Sec. 3) or measuring the overdensity factor (Sec. 4.1). Instead, all galaxies are retained to represent the underlying galaxy clustering in our sample.

3. SYSTEMATIC SEARCH FOR OVERDENSITY CANDIDATE

In order to identify overdensities within our sample, it is important to quantify the local galaxy densities and investigate how galaxy parameter relate to their local environments. This can be done by reconstructing a galaxy overdensity map, either by creating a comprehensive 3D map or by slicing it into a 2D map by using a redshift slice. A 2D map is suitable for the photometric redshift sample because of their large redshift uncertainties. The framework for this map construction is presented below and illustrated in Figure 3. We will refer to the numbered blocks in the flowchart as *Step N* throughout this section.

3.1. Redshift Slices

We consider the selection of redshift slices used to create the 2D overdensity map in each field. Previous studies defined their redshift slice width based either on the photometric redshift uncertainty (B. Darvish et al. 2015) or on the comoving size ($\Delta\chi$) of galaxy clusters accounting for redshift-space distortion (RSD) effects (e.g., N. Chartab et al. 2020; S. Taamoli et al. 2024). We explore both approaches. We first evaluate the photo-z-based approach. The typical redshift uncertainty of our sample is estimated from 20 BEACON fields, we defined this uncertainty as the median absolute deviation of the normalized redshift error, $\Delta z = (z_{84} - z_{16})/(1 + z_{\text{phot}})$, where z_{16} and z_{84} represents the 16th and 84th percentiles of the photometric redshift distribution, which results in $\sigma_z = 0.07$ across all redshifts. This corresponds to comoving scales of $\Delta\chi \sim 90$ cMpc at $z = 1.5$ and ~ 25 cMpc at $z = 5.0$.

Alternatively, we consider a physically motivated approach based on the expected size of massive protoclusters. The corresponding redshift width at a given redshift can be calculated as

$$\Delta z = \frac{\Delta\chi H_0}{c} \sqrt{\Omega_m(1+z)^3 + \Omega_\Lambda}. \quad (4)$$

We adopt a fixed comoving width $\Delta\chi = 20$ cMpc, which corresponds to the predicted spatial extent of the most massive (Coma-like) protoclusters at $z \sim 5$ (Y.-K. Chiang et al. 2013). However, this width corresponds to a median redshift slice of $\sigma_z \simeq 0.03$, considerably smaller than the typical photometric redshift uncertainty of our sample. To evaluate the impact of slice width, we run our overdensity mapping algorithm using both $\Delta\chi = 20$ cMpc and $\Delta\chi = 90$ cMpc. We find that the choice of redshift slice width does not significantly affect the resulting overdensity maps within our uncertainties, as it does not alter the spatial distribution of overdense regions nor the derived overdensity values, consistent with the findings of K. Shi et al. (2024). Therefore, to maintain finer redshift resolution in our final maps and catalogs, we adopt a comoving width of $\Delta\chi = 20$ cMpc for the redshift slice definition. We perform the calculation from $z = 1.5$ to $z = 7.0$, resulting in 214 redshift slices in total.

For each redshift slice with $z \in [z_a, z_b]$, the weight of each galaxy can be calculated as

$$w = \int_{z_a}^{z_b} P(z) dz \quad (5)$$

(Step 1 in Figure 3).

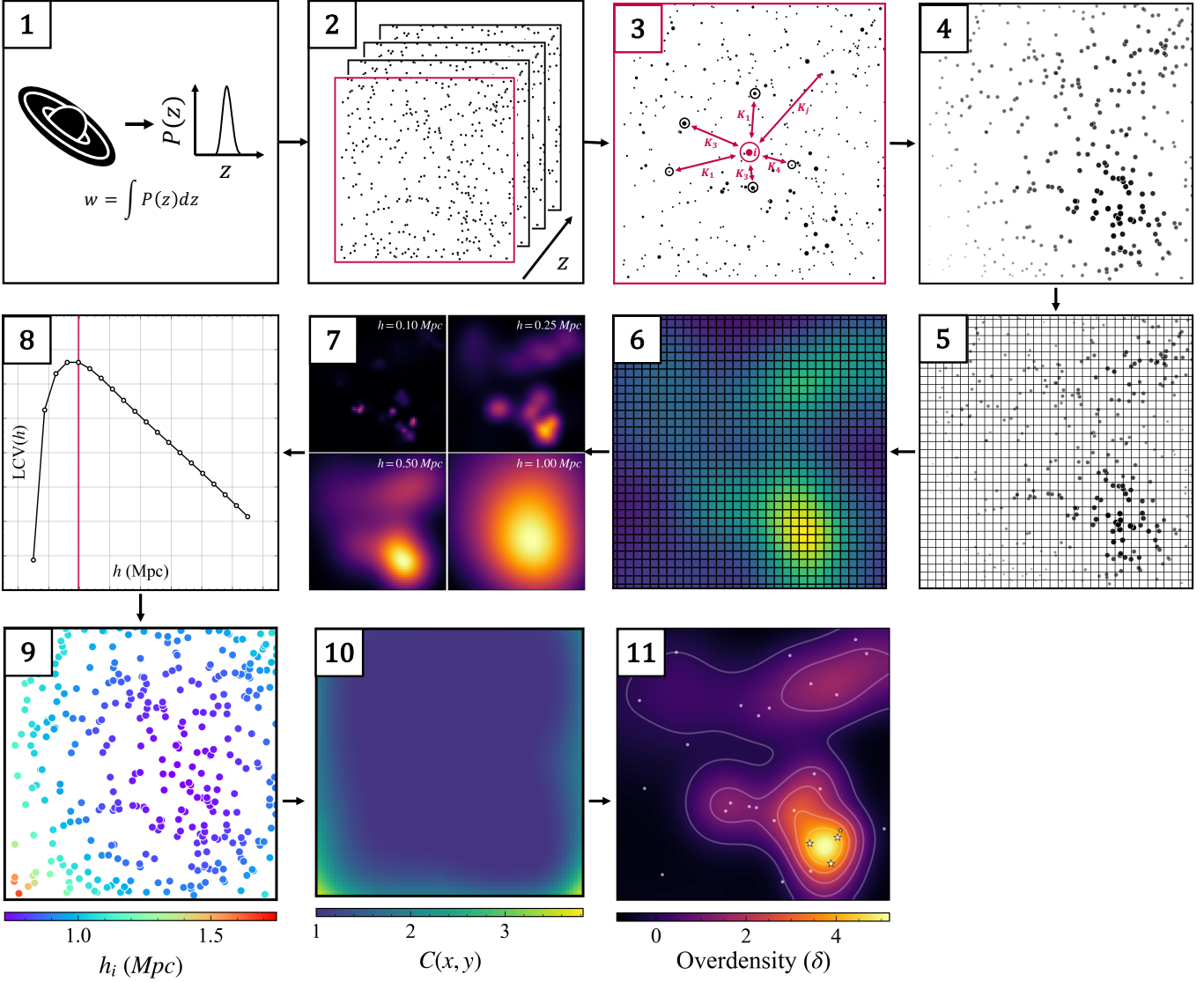


Figure 3. The flowchart of the overdensity map creation, following the direction of arrows. (1) Weighting of each galaxy is calculated by its photometric redshift PDF. (2) Each field is divided into redshift slices following the definition from Section 3.1 (3) For each slice (red box), calculate surface density using Equation 6 around each galaxy (red dot) based on all surrounding galaxies. Different dot sizes represent different weights. (4) The surface density of each galaxy, where larger size and opacity corresponds to larger local surface density. (5) Dividing the mosaic into defined pixel grid. (6) Calculation on each pixel grid (x, y) following Equation 11. (7) Iterative calculation of global bandwidth. (8) Optimal global bandwidth selection based on LCV. (9) Map of local bandwidth of each galaxy calculated with $h_i = h \times \lambda_i$. (10) Edge correction factor map. (11) The final overdensity map with contour step of $\Delta\delta = 1$. Each data point corresponds to galaxies that are located inside the redshift slice. Star markers show galaxies that are spatially included in the overdense region.

3.2. Weighted-Adaptive Kernel Density Estimation

We apply the weighted adaptive kernel density estimation (wKDE) introduced by B. Darvish et al. (2015). This can be done by performing an iterative procedure of adjusting parameters adaptively to calculate the surface density, following the N. Chartab et al. (2020) workflow, with some modifications. Unlike the standard calculation of kernel density estimation (KDE), this method applies the weight of galaxies based on their full PDF

with an adaptive algorithm to adjust the creation of the surface density map. The adaptive algorithm takes place in two parts, applied for calculating the smoothing parameter for the map, globally on each redshift slice, and locally at each galaxy location based on its local density.

For each redshift slice z (Step 2), we estimate the local surface density (σ_i) for each galaxy i , based on the sum of the kernel with the other galaxies j in our sample and

their weight w_j calculated by the redshift PDF (Step 3),

$$\sigma_i = \frac{1}{\sum_{j=1, j \neq i}^N w_j} \sum_{j=1, j \neq i}^N w_j K(\mathbf{r}_i, \mathbf{r}_j, h) \quad (6)$$

where N is the number of galaxies in the sample, K is the kernel function, defined by the position of the galaxy i (\mathbf{r}_i) and the rest j (\mathbf{r}_j), with h as the bandwidth of the kernel function, which provides the smoothing parameter for density maps. The σ_i is calculated for every galaxy inside the sample, on every redshift slice (Step 4).

We choose a 2D symmetric Gaussian kernel, considering each NIRCam mosaic is small enough for a circular kernel (e.g., the von Mises kernel) to be used. A 2D symmetric Gaussian kernel is defined as:

$$K(\mathbf{r}_i, \mathbf{r}_j, h) = \frac{1}{2\pi h^2} \exp\left(-\frac{|\mathbf{r}_i - \mathbf{r}_j|^2}{2h^2}\right) \quad (7)$$

In this case, when calculating the local surface density for each galaxy σ_i , we first have to define a global kernel bandwidth (h) for each redshift slice. It is possible to choose a specific well-established value based on the observation, such as the typical size of the local clusters, as adopted by [B. Darvish et al. \(2015\)](#), by choosing $h = 0.5$ Mpc, which corresponds to the typical value of R_{200} for X-ray clusters and group in the COSMOS field. However, this specific value might be unsuited in our study, due to potentially our lower-mass limit, observational setup, and redshift range. Therefore, we need to choose our own global bandwidth.

It is important to keep the bias-variance tradeoff in the sense that choosing too narrow a bandwidth could give rise an overestimate of variance (undersmoothing), which shows unrelated detailed features (e.g., shot noise) in the density map, while choosing too wide a bandwidth could give rise to a high-bias map (oversmoothing), which creates a too simple map by removing important finer features ([B. Darvish et al. 2015](#); [N. Chartab et al. 2020](#)). In this sense, the choice of global bandwidth must depend only on the distribution of the sample across the mosaic.

Therefore, we employ Likelihood-Cross Variance (LCV) ([P. Hall 1982](#); [N. Chartab et al. 2020](#)), to choose the best global width for each redshift slice. The calculation is done iteratively by grid-searching the global bandwidth value that maximizes the likelihood value, based on our data (Step 7-8). LCV is defined as:

$$LCV(h) = \frac{1}{N} \sum_{k=1}^N \log(\sigma_{-k}(\mathbf{r})) \quad (8)$$

where N is the total number of galaxies in the sample, and σ_{-k} is the surface density for galaxy k excluding

itself, which is already calculated by Equation (6). We obtain typical value of $h = 0.28$ (1.50) cmpc at $z = 1.5$ (7.0). This calculation marks the first adaptive part.

Within each redshift slice, different regions of the mosaic may have a variety of local densities. Therefore, we cannot directly apply the LCV-chosen global bandwidth to the final calculation, as it will cause the problem of map creation previously discussed. Thus, we also use the second adaptive part by adjusting the global bandwidth h to each galaxy based on its local density (Step 9), defined as local bandwidth $h_i = h \times \lambda_i$, where λ_i is proportional to the inverse of local density ([I. S. Abramson 1982](#); [B. W. Silverman 2018](#); [B. Darvish et al. 2015](#)),

$$\lambda_i = \left(\frac{G}{\sigma_i}\right)^{0.5} \quad (9)$$

where G is the geometric mean of all the estimated σ_i values, defined as,

$$\log(G) = \frac{1}{N} \sum_{i=1}^N \log(\sigma_i) \quad (10)$$

In order to construct a complete map of each redshift slice, we can calculate the surface density on each pre-defined 2D grid, $r = (x, y)$, on the mosaic, either on each pixel or pixel bin, that is group of pixels that are binned together, similar to Equation 6,

$$\sigma(x, y) \equiv \sigma(\mathbf{r}) = \frac{1}{\sum_{i=1}^N w_i} \sum_{i=1}^N w_i K(\mathbf{r}, \mathbf{r}_i, h_i) \quad (11)$$

We perform a calculation on the 50 kpc pixel binning (Step 5-6). This corresponds to $2.^{\circ}3$ ($1.^{\circ}2$) at $z = 1.5$ (7.0). We adopt this choice by considering this scale is larger than galaxy sizes but much finer than the global bandwidth and typical cluster scale.

3.3. Edge Correction

[N. Chartab et al. \(2020\)](#) and [S. Taamoli et al. \(2024\)](#) addressed the problem of calculating the surface density on the edge of the data mosaic using the kernel density estimation algorithm. The kernel function is continuous. On the limited or bounded data, the kernel density estimation encounters a discontinuity and spillover to the region outside the boundary, which causes bias at and near edges of the data. This effect is referred to as the boundary effect.

The actual survey is always limited by the instrument field of view, which serves as the boundary to the kernel density estimation. This limitation can cause an underestimation of the surface density at the edge of the mosaic, introduced by the boundary effect. This problem can be easily addressed in a large field by cutting the

edge part, because the edge region is small compared to the whole survey area and does not significantly affect the overall map. However, it is crucial to account for the boundary effect in parallel surveys, such as ours, as the random pointings increase the edge over area ratio.

There are various ways to perform the edge correction introduced by the boundary effect, namely the reflection method (E. F. Schuster 1985), the renormalization method (P. Diggle 1985; M. C. Jones 1993), the transformation method (J. S. Marron & D. Ruppert 1994), the local polynomial method (M. C. Jones 1993; M.-Y. Cheng 1997), the pseudo-data method (A. Cowling & P. Hall 1996), and the boundary kernel methods (H.-G. Müller 1991; S. X. Chen 1999, 2000).

We adopt the renormalization method, which is the most intuitive and computationally efficient approach to correct for edge effects on the density map, following N. Chartab et al. (2020), and originally formulated by M. C. Jones (1993). In this method, the integral of each kernel is normalized to unity, ensuring that the estimated surface density remains unbiased even near the survey boundaries.

Near the edges, the kernel function is truncated by the boundaries, resulting in a non-unity surface integral:

$$N(x, y) \equiv N(\mathbf{r}) = \int_S K(\mathbf{r}, \mathbf{r}_i, h_i) < 1. \quad (12)$$

where $N(x, y)$ is the integrated kernel normalization evaluated at position (x, y) within the valid region of the field S . Thus, the expectation value of the estimated surface density becomes

$$\mathbf{E}[\sigma(x, y)] = N(x, y) \sigma_{\text{True}}(x, y) \quad (13)$$

Therefore, to remove this bias and recover an unbiased estimate, we can define the correction factor as the inverse of the kernel normalization:

$$C(x, y) = \frac{1}{N(x, y)} \quad (14)$$

and apply it to the surface density calculation:

$$\sigma_{\text{corr}}(x, y) = C(x, y) \sigma(x, y) \quad (15)$$

The correction factor, $C(x, y)$, ranges from approximately 1 at the center of the density map to about 3.5 near the field boundaries (Step 10). Hence, ignoring the boundary effect can lead to an underestimation of the surface density by up to a factor of 3.5, consistent with the findings of N. Chartab et al. (2020).

4. GALAXY OVERDENSITIES FROM NIRCAM PURE-PARALLEL FIELDS

4.1. Identifying Overdensities

We calculate the overdensity factor (δ) at each location $r = (x, y)$ by defining,

$$\delta(x, y) = \frac{\sigma(x, y)}{\bar{\sigma}} - 1 \quad (16)$$

where $\bar{\sigma}$ is the median value of σ at each redshift slice (Step 11). We discuss how we determine the median sigma for our calculation in the Appendix A. We show an example of an overdensity map in Figure 4.

We note that at higher redshifts the overdensity factor becomes increasingly uncertain due to the limited field of view and the decreased number of detected galaxies, which results in an insufficient reference sample of field galaxies. We therefore emphasize that our method is unsuitable for estimating the overdensity factor in small fields at high redshift. Instead, estimating the overdensity factor through a comparison with the expectation number from luminosity function offers more reliable results (e.g., Y. Zhang et al. 2026; K. C. Kreilgaard et al., in preparation).

In addition, the overdensity factor calculated using this method includes photometric redshift uncertainties, which incorporate the photo- z blurring effect. This can cause the overdensity factor to be underestimated relative to its true value, particularly in cases where the overdensities correspond to real physical structures.

From these obtained maps, we select galaxy overdensities by applying the following criteria:

1. The peak of the overdensity should be at least above 4σ , following M. Brinch et al. (2023). This threshold is also supported by the simulation study of J. Toshikawa et al. (2016), which shows that 76% of systems satisfying this criterion will evolve into actual galaxy clusters by $z = 0$, with halo masses $M_h(z = 0) \geq 10^{14} M_\odot$.
2. Potential galaxy members should be above the magnitude limit (Sec. 2.5) and located within the 1σ overdensity contour.
3. The probability that a galaxy resides within the overdensity, based on its photometric redshift PDF, is at least 68% within the 1σ redshift interval around the center of the overdensity.
4. The overdensity contains at least 7 potential galaxy members, in order to remove spurious detection.

Lastly, we merge duplicated overdensity in the same field, if those are within $\Delta z < 0.1$ and the projected distance between the centroids is $< 1 \text{ cMpc}$. We initially

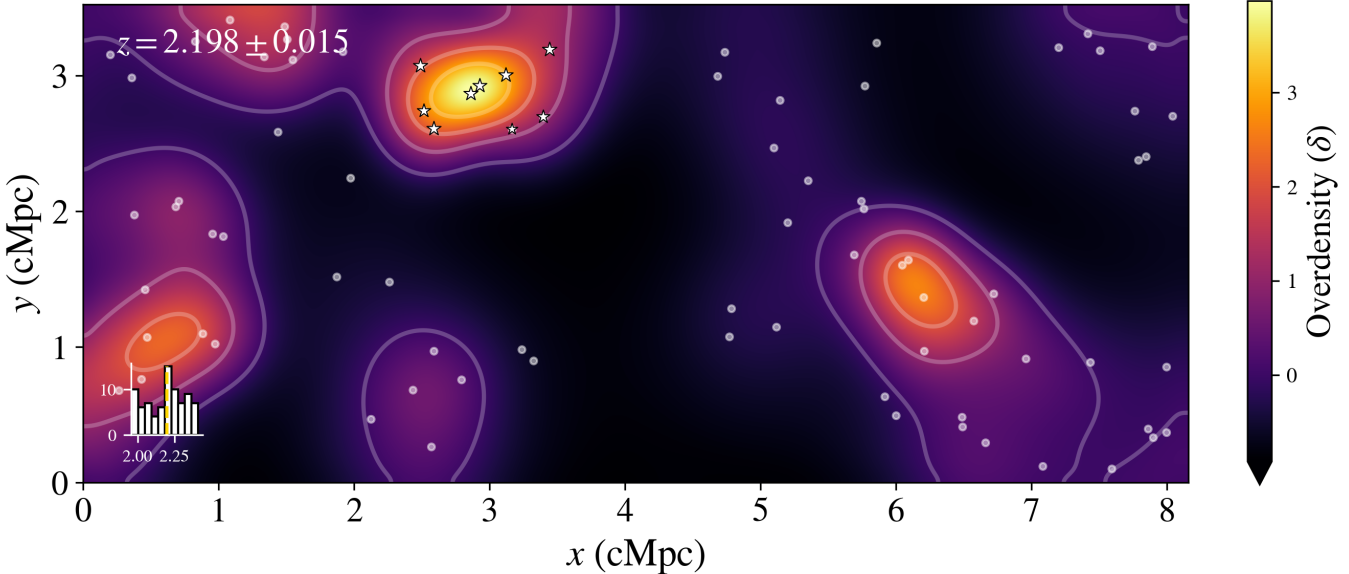


Figure 4. Example of a two-dimensional overdensity map of the beacon_0055-3749 field at $z = 2.20$. The map is plotted in the x - y plane, converted into comoving coordinates in the unit of cMpc. White contours indicate one-step increments of the overdensity factor (δ). White dots mark galaxies that have a probability of being included within the map, accounting for their photometric redshift uncertainties. The star symbols denote galaxies located within the $> 1\sigma$ overdensity contour, representing the probable members of the overdense region. The inset panel in the bottom-left corner shows the photometric redshift distribution of galaxies within the redshift slice.

obtain 1432 overdensities with a significant number of galaxy members ($n_{gal} > 7$), where this number still suffers from the duplication problem. After performing the merging step, we obtain a clean sample of 207 overdensities.

4.2. Estimating Halo Mass

The total halo mass of each identified overdensity can be estimated by summing the halo masses of its member galaxies, which may be derived using several approaches. The most commonly adopted method relies on the stellar-to-halo mass relation (SHMR), obtained from empirical abundance-matching models (P. S. Behroozi et al. 2013; P. Behroozi et al. 2019; M. Shuntov et al. 2025) or halo occupation distribution (HOD) frameworks (M. Shuntov et al. 2022). A simpler alternative involves a direct conversion from stellar (or baryonic) mass to halo mass by assuming a fixed baryon-to-dark matter fraction and a one-to-one correspondence between galaxies and halos (N. Laporte et al. 2022; C. K. Jespersen et al. 2025; M. Brinch et al. 2023). In addition, halo masses may be inferred using empirical relations tied to other galaxy properties, such as the M_h - M_{UV} relation (C. A. Mason et al. 2023).

However, the relations derived from the analytical SHMR equation (P. S. Behroozi et al. 2013) or the interpolation of the stellar mass-halo mass ratio (M. Boquien et al. 2019) do not extend to the massive end at $z > 2$. In

these relations, the halo mass reaches a peak at a stellar mass of approximately $M_* \sim 10^{10.5}-10^{11} M_\odot$, and begins to decline at higher halo mass. Thus, these relations are not suitable for our stellar mass distribution, which extends up to $\sim 10^{12} M_\odot$.

To overcome this problem, we use the updated observed stellar-to-halo mass relation derived by M. Shuntov et al. (2025) using the COSMOS-Web JWST catalog, which incorporates ancillary imaging, ensuring a highly complete sample even at the lower mass end. M. Shuntov et al. (2025) provide the stellar-to-halo mass relation for massive-end galaxies and extend the relation up to $z \sim 10$.

Considering the stellar mass uncertainties derived from SED fitting, we perform a bootstrapping method to estimate the overdensity's halo mass. For each bootstrapping realization, we randomly select the mass of each potential galaxy member by assuming a Gaussian distribution posterior centered around the Bayesian stellar mass, with uncertainties derived by CIGALE as the standard deviation. These randomly selected masses are then incorporated into the calculation of the total halo mass of the system.

The total halo mass of each overdensity can be determined by integrating the individual potential galaxy member halo masses, which are derived by interpolating individual galaxy SED-derived stellar masses with the M. Shuntov et al. (2025) stellar-to-halo mass rela-

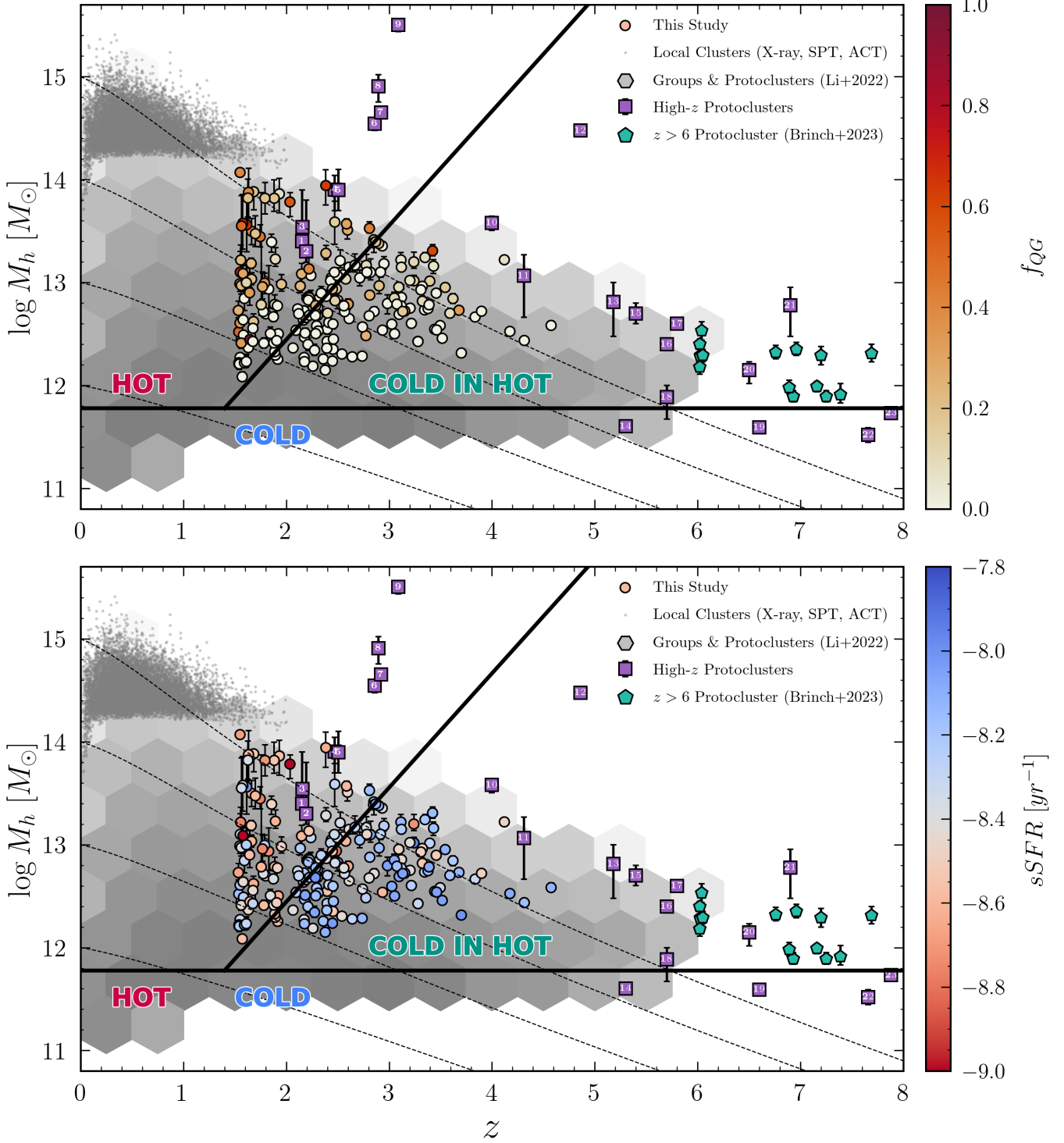


Figure 5. The distribution of halo mass of our overdensities as a function of redshift. Error bar represents 1σ error of the halo mass estimation from bootstrapping. Solid circle: data points from this study, color-coded by their measured quiescent galaxy fraction (top) and median of specific star formation rate (bottom). Solid lines: dividing lines of the halo accretion modes to cold, hot, and cold in hot modes as predicted by A. Dekel & Y. Birnboim (2006). Dashed lines: median halo mass growth history for each present-day halo with a masses of $\log(M_h(z=0)) = 12.0, 13.0, 14.0$, and 15.0 , derived by P. S. Behroozi et al. (2013). Small gray dot: local clusters detected with Sunyaev-Zel'dovich (SZ) effects with ROSAT All-Sky Survey (X-ray) or Planck Satellite (FIR) (P. Tarrío et al. 2019), South Pole Telescope (SPT; S. Bocquet et al. 2019), and Atacama Cosmology Telescope (ACT; ACTDESHEC Collaboration et al. 2025). Grey hex-plots: groups and protoclusters identified by Q. Li et al. (2022) using halo-based group finder. Pentagon (green): protocluster candidates from M. Brinch et al. (2023) using a similar method to this study. Square (purple): high redshift protoclusters compiled from various studies. See Section 4.2 for detailed references.

tion. We perform 100 bootstrap realizations for each overdensity and present its final halo mass as the median of the distribution, along with its 1σ error derived from the 68% percentile of the distribution. The final result is presented in Figure 5. However, since the galaxies involved in this work is incomplete below the stellar-mass completeness limit, our halo mass estimates are dominated by the most massive member galaxies, rather than a fully complete total halo mass.

For comparison, we also include various protoclusters and galaxy systems reported in previous studies, identified through different methods, compiled in [R. A. Overzier \(2016\)](#). At low redshift, we show galaxy clusters detected via the Sunyaev–Zel'dovich (SZ) effect using X-ray observations from the Planck satellite and the ROSAT All-Sky Survey (RASS), compiled by [P. Tarrío et al. \(2019\)](#). At intermediate redshifts, we compare galaxy groups and protocluster candidates identified using photometric and spectroscopic samples from [Q. Li et al. \(2022\)](#), based on the halo-based group finder ([X. Yang et al. 2007](#)). Our galaxy systems are distributed consistently with these group and protocluster candidates.

We also include high-redshift ($z > 6$) protoclusters in [M. Brinch et al. \(2023\)](#), identified through similar techniques to our study. In addition, we compare with various well-known protoclusters reported in the literature, including: (1–2) PHz_G237.01+42.50 ([Y. Koyama et al. 2021](#); [M. Polletta et al. 2021](#)), (3) the Spiderweb protocluster ([L. Di Mascolo et al. 2023](#)), (4) PCL1002 ([C. M. Casey et al. 2015](#)), (5) CLJ1001 ([T. Wang et al. 2016](#)), (6–7) MRC0052–241 and MRC0943–242 ([B. P. Venemans et al. 2007](#)), (8) P2Q1 ([O. Cucciati et al. 2014](#)), (9) SSA22 ([M. W. Topping et al. 2018](#)), (10) DRC protocluster ([I. Oteo et al. 2018](#)), (11) SPT2349–56 ([T. B. Miller et al. 2018](#)), (12) SDF_z47 ([J. Toshikawa et al. 2014](#)), (13) HDF850.1 ([F. Sun et al. 2023](#)), (14) COSMOSAzTEC03 ([P. L. Capak et al. 2011](#)), (15) JADES-GDSz5p4 ([J. M. Helton et al. 2024](#)), (16–17) A2744-ODz5p7 and A2744-ODz5p8 ([T. Morishita et al. 2025a](#)), (18–19) z57OD and z66OD ([Y. Harikane et al. 2019](#)), (20) the system reported by [K. Chanchaiworawit et al. \(2019\)](#), (21) SPT0311–58 ([S. Arribas et al. 2024](#)), (22) SMACS0723–7327 ([N. Laporte et al. 2022](#)), and (23) A2744-ODz7p9 ([T. Morishita et al. 2023, 2025c](#)).

Overall, our galaxy overdensity samples lie above $M_h \sim 10^{12} M_\odot$, with the most massive mass reaching $\sim 10^{14} M_\odot$ at $z \simeq 1.5$. Our sample exhibits a right-wedge-like distribution in the halo mass–redshift plane, consistent with the groups and protoclusters identified by [Q. Li et al. \(2022\)](#), despite differences in identification methods.

The relatively flat distribution at lower halo masses can be explained by our selection approach, where we apply a constant overdensity significance threshold (σ_δ) that is independent of redshift. However, the same overdensity factor may represent different physical conditions at different epochs. The galaxy overdensity (δ_{gal}) is proportional to the underlying matter overdensity (δ_m). Under gravitational evolution, these structures undergo spherical collapse and grow over time. Consequently, an identical overdensity factor at higher redshift corresponds to a system that will evolve into a more massive halo at the present day ([Y.-K. Chiang et al. 2013](#); [R. A. Overzier 2016](#)).

At the high-mass end, our sample follows the trend predicted by the median halo mass accretion history from [P. S. Behroozi et al. \(2013\)](#), consistent with present-day halos of $M_h(z=0) \sim 10^{15} M_\odot$.

Finally, the distribution of our galaxy overdensities is above the theoretical shock-heating threshold (M_{shock}) and divided by the predicted cold-stream and hot-halo regions defined in [A. Dekel & Y. Birnboim \(2006\)](#). We further investigate the differences in galaxy system properties between these two regimes.

4.3. Notable Examples

Here, we present a few notable examples of the galaxy overdensities that can be classified as protocluster candidates, defined by their present day halo mass $M_h(z=0) \geq 10^{14} M_\odot$, assuming these systems evolve following the average halo mass growth trajectories ([Y.-K. Chiang et al. 2013](#); [P. S. Behroozi et al. 2013](#)). We present three galaxy overdensities of interest in this section in three categories: most massive system, highest quiescent fraction system, and highest overdensity factor system. For each of these systems, the density map and potential galaxy members snapshot is presented in Figure 6.

4.3.1. Most Massive System: BEACON_2325-1203_z1.55

We identify BEACON_2325-1203_z1.55 as the most massive overdensity in our sample. The structure lies at $z = 1.55$ and exhibits a peak overdensity of $\delta = 7.4$ (corresponding to 10.5σ). The density map shows that the 29 potential member galaxies are grouped in three distinct peaks, two of which exhibit elongated morphologies, suggesting the presence of filamentary structures connected to the system (Figure 6). Of these galaxies, 13 lie within the 4σ contour.

The system hosts a total stellar mass of $1 \times 10^{12} M_\odot$, which corresponds to an estimated halo mass of $1.2 \times 10^{14} M_\odot$. Under classical definitions, such a mass scale is consistent with a galaxy cluster. As shown in Figure 5, this can be associated with the local clusters distributions. However, this claim must remain speculative

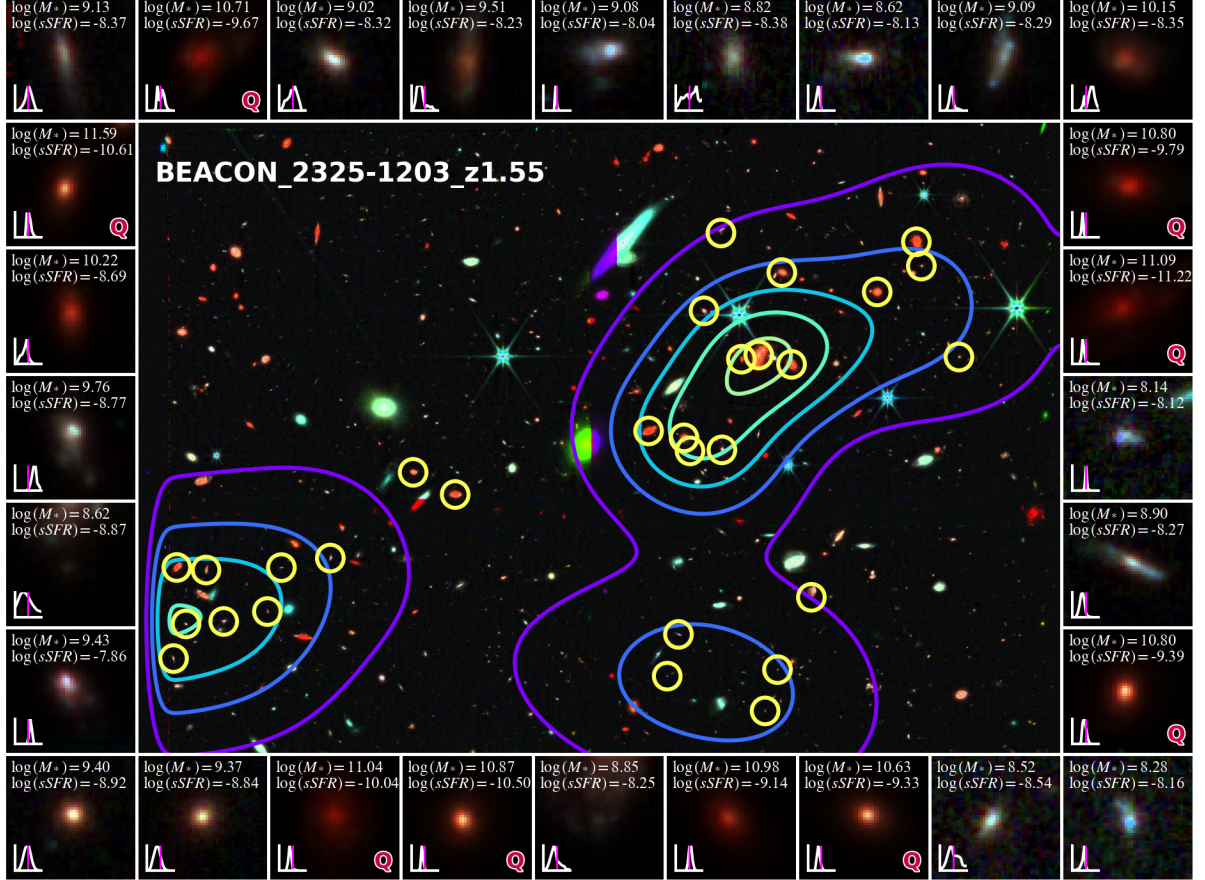


Figure 6. The snapshots of three examples of overdensities and their galaxy member candidates. Each panel shows each overdensity that described in Section 4.3. Yellow circles represent the potential galaxy member in each galaxy system. Each small panel surrounding the main panels shows snapshots of each individual galaxy member, along with its derived stellar mass and sSFR. UVJ-selected quiescent galaxies are marked with “Q”. The histogram in the bottom-left corner of each small panel shows the photo- z PDF, with a pink vertical line indicating the redshift of the respective overdensity. Contours on the main panels have different increments: $\delta = 1$ step (top two panels) and $\delta = 2$ (bottom panel). This figure is a snapshot for the most massive system: BEACON_2325-1203_z1.55

in the absence of actual spectroscopic confirmation or independent evidence from SZ or X-ray observations.

The system includes eight notable massive quiescent galaxies ($M_* \geq 10^{10.5} M_\odot$), indicating a relatively evolved population already present at this epoch. The overdensity spans a projected comoving extent of 2.5×3.5 cMpc.

4.3.2. Highest Quiescent Fraction: BEACON_0447-2637_z2.00

We identify BEACON_0447-2637_z2.00, located at $z = 2.00$, as the overdensity with the highest quiescent fraction of 45% with 11 potential galaxy members. The density map shows that the potential member galaxies are concentrated in a compact cluster, with a projected size of 2×2 cMpc. The system exhibits a peak overdensity of $\delta = 6.6$ (9.3σ). Of the 11 identified potential galaxy members, 6 are located above the 4σ contour,

including 5 of the massive quiescent galaxies mentioned previously.

The system hosts a total stellar mass of $6.6 \times 10^{11} M_\odot$, which corresponds to an estimated halo mass of $5.1 \times 10^{13} M_\odot$. Assuming this overdensity to evolve following the average mass growth, it will become a Coma-type cluster ($M_h \geq 10^{15} M_\odot$) at the present day.

The galaxy members span stellar masses from $10^9 M_\odot$ to $10^{11.5} M_\odot$. Notably, all five galaxies with $M_* \geq 10^{10.5} M_\odot$ in this system are classified as quiescent galaxies, yielding a quiescent fraction of 100% above this mass limit. To place this result in context, we compare the quiescent fraction in this system with previous studies of field galaxy populations. Using the stellar mass functions (SMFs) of total and quiescent galaxies from O. Ilbert et al. (2013), A. Muzzin et al. (2013), and J. Weaver et al. (2023), we derive the field quiescent fraction at $2 <$

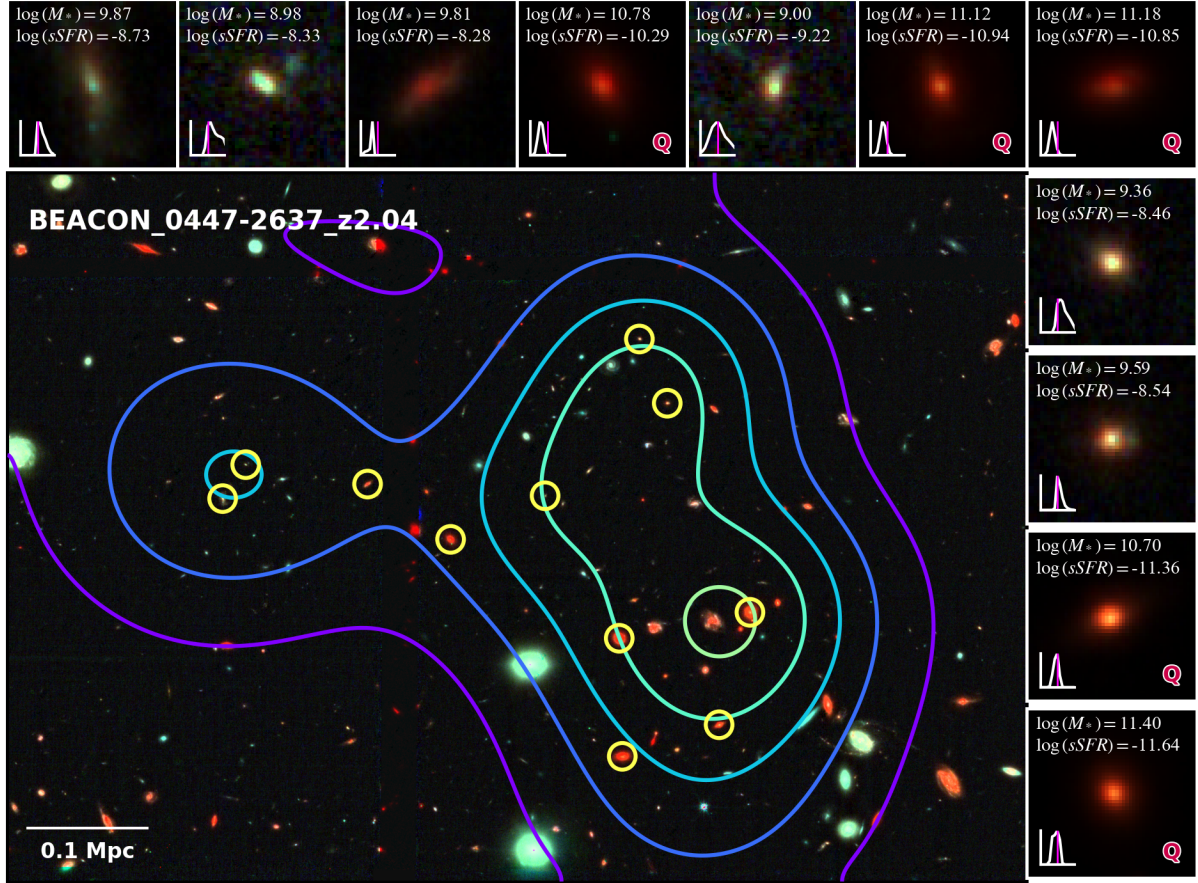


Figure 6. Continued. This figure is a snapshot for the highest quiescent fraction system: BEACON_0447-2637_z2.00

$z < 2.5$ by integrating the SMFs above $M_* > 10^{10.5} M_\odot$. This yields $f_Q(> 10^{10.5}) = 23\%, 24\%$, and 21% for each study, respectively. For J. Weaver et al. (2023), whose mass completeness extends to lower stellar masses, we additionally compute $f_Q(> 10^9) = 3.2\%$. This value is broadly consistent with the quiescent fraction measured in our sample, for which we find $f_Q(> 10^9) = 4.2\%$.

Compared to these field benchmarks, BEACON_0447-2637_z2.00 shows a quiescent fraction about five times higher at the massive end, strongly suggesting the presence of environmentally driven quenching, particularly among massive galaxies. Similar results have been reported in previous studies of clusters at comparable redshifts; for example, quiescent fractions among massive galaxies ($> 10^{11} M_\odot$ in $z \sim 1.8$ clusters) have been found to reach values as high as 100% (A. B. Newman et al. 2014). We further compare our result to the protocluster SMF presented by A. H. Edward et al. (2024), derived from protoclusters at $2 < z < 2.5$, which yields a protocluster quiescent fraction of 57%.

Together, these comparisons indicate that environmental quenching may already be underway by $z \sim 2$, and BEACON_0447-2637_z2.00 represents an extreme

case among high-redshift overdensities in terms of its quiescent galaxy population. Similar findings at $z \sim 2-3$ have also been reported by K. Ito et al. (2023) and I. McConachie et al. (2022).

4.3.3. Highest Overdensity Factor: BEACON_0332-2745_z3.32

We identify BEACON_0332-2745_z3.32 as the overdensity with the highest overdensity factor of $\delta = 25.0$, corresponding to 32σ , which lies at $z = 3.32$. The density map shows that the potential member galaxies are distributed into one compact clustering, with another small clustering on the other side, covering total projected size of 3×2.4 cMpc.

The system hosts a total stellar mass of $3.6 \times 10^{10} M_\odot$, which corresponds to an estimated halo mass of $5.0 \times 10^{12} M_\odot$. We identify 20 potential galaxy members, of which 9 lie within the 4σ contour. All of the potential galaxy members are classified as star-forming galaxies, marking the early phase formation of the galaxy overdensity, a stark contrast to the highly quiescent system BEACON_0447-2637_z2.00 at lower redshift.

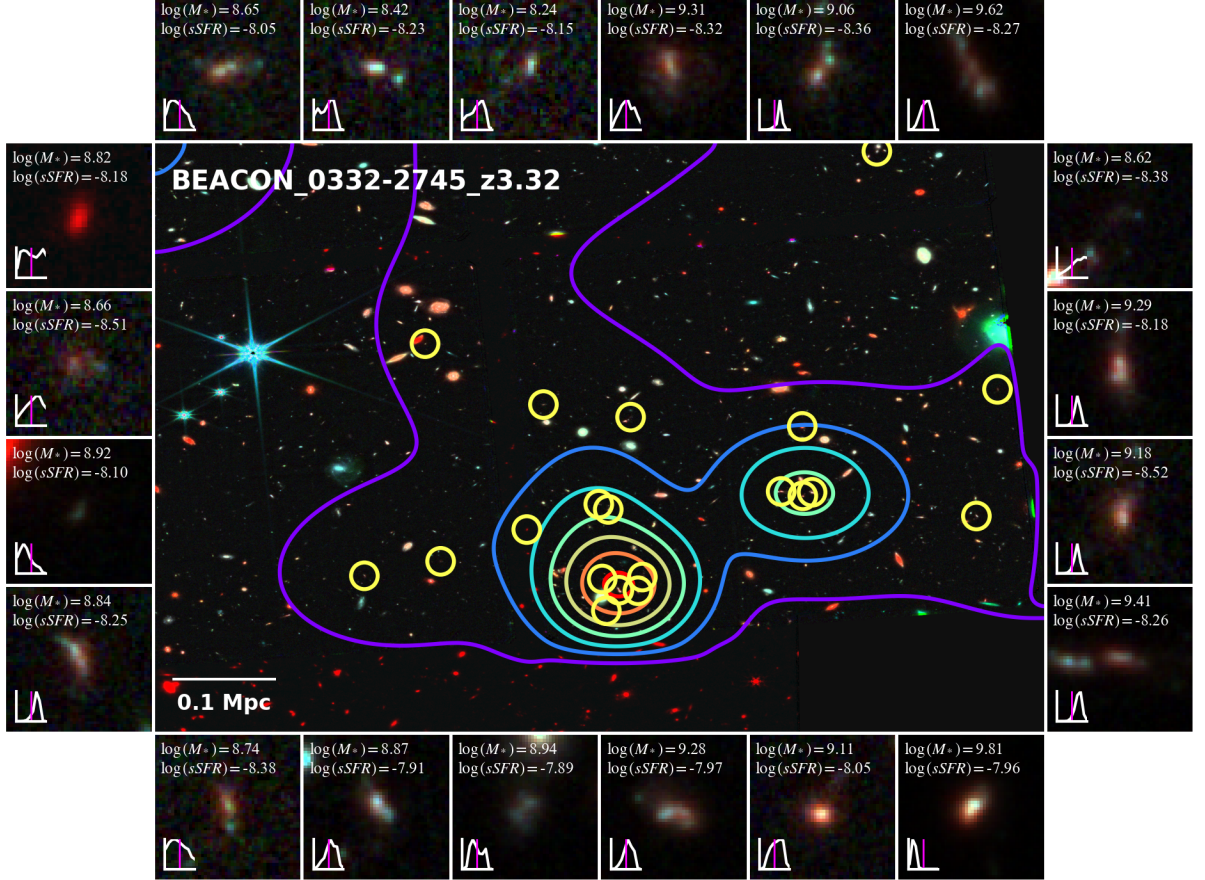


Figure 6. Continued. This figure is a snapshot for the highest overdensity factor system: BEACON_0332-2745_z3.32

4.4. Galaxy Properties with Respect to Their Environment

For each identified overdensity presented in Figure 5, we calculate quiescent galaxy fraction based on the potential galaxy member and apply a color coding on each system. Additionally, we also apply a color coding based on *sSFR* which is represented by its median in the lower panel of Figure 5.

To complement our analysis on how galaxy properties evolve with respect to their global system characteristics, we examine how individual galaxy properties vary with their local environment. Specifically, we investigate the evolution of the quiescent galaxy fraction (f_{QG}), stellar mass (M_*), and specific star formation rate (*sSFR*) as a function of local overdensity (δ), as shown in Figure 7. To trace their evolution over cosmic time, we divide the sample into redshift bins corresponding to roughly 1 Gyr intervals: $1.5 < z < 2$, $2 < z < 3$, and $3 < z < 5$.

For each redshift bin, the quiescent galaxy fraction is computed within bins of overdensity, considering only galaxies above the stellar mass completeness limit. The

associated uncertainties are derived using the binomial confidence interval from [E. B. Wilson \(1927\)](#). The stellar mass and *sSFR* distributions are represented by their median values, with 1σ scatter estimated from their standard deviations. In each panel, we also display the best-fit linear relation and its 1σ uncertainty.

To assess the strength and significance of these correlations, we compute the Kendall rank correlation coefficient ([M. G. Kendall 1938](#)). We further account for the measurement uncertainties of each data point through a Monte Carlo error propagation approach following [P. A. Curran \(2014\)](#). The resulting correlation coefficients and their statistical significance are summarized in Table 1.

From Fig. 7 and the Kendall's τ values for each parameter, we find that the trends of f_{QG} and M_* steepen toward lower redshift. As a result, these correlations become statistically significant at $z < 2$. In contrast, *sSFR* shows a different behavior along redshift. While it is negatively correlated with local density at $z < 2$, which is qualitatively consistent with the other two parameters, it exhibits a reversal toward a positive correlation at higher redshift, although this trend remains statisti-

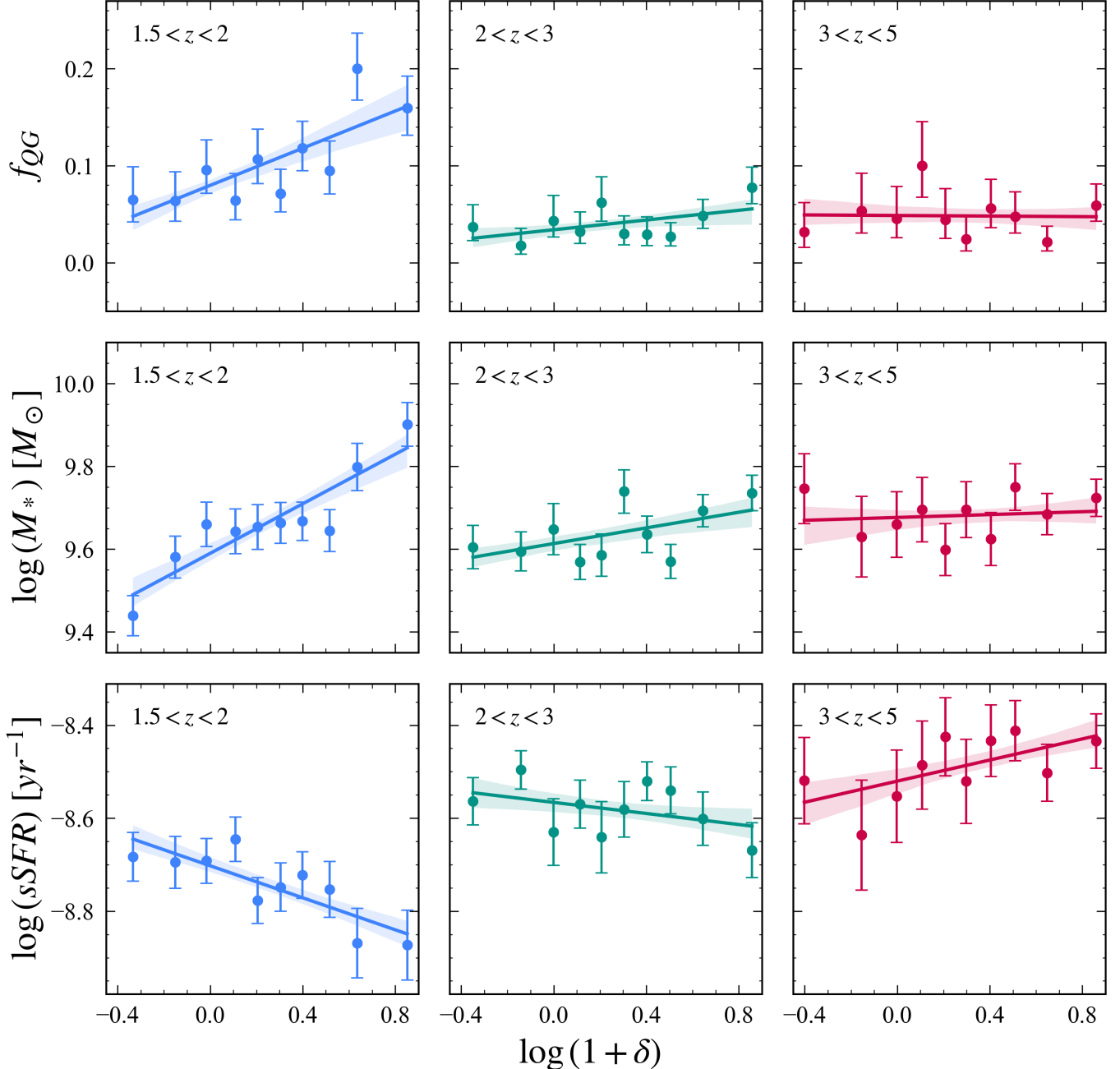


Figure 7. Galaxy properties as a function of local density for the quiescent fraction (top), stellar mass (middle), and sSFR (bottom), represented by the median value on each bin.

cally weak. We will revisit this in Discussion (Section 5.2).

5. DISCUSSION

We investigate how the properties of galaxies in overdense regions are influenced by two scales: global environment, characterized by the total (halo) mass (M_h), and local environment, characterized by the overdensity factor (δ).

5.1. Properties of Systems with Respect to Their Halo Masses and Redshifts

[A. Dekel & Y. Birnboim \(2006\)](#) proposed that star formation activity in galaxies is regulated by the mode of gas accretion, which depends on the thermodynamic properties of the host halo and eventually gives rise to the observed galaxy bimodality. Halos below a critical shock-heating mass, $M_h < M_{\text{shock}} \approx 6 \times 10^{11} M_\odot$, are expected to accrete gas in the cold mode, where

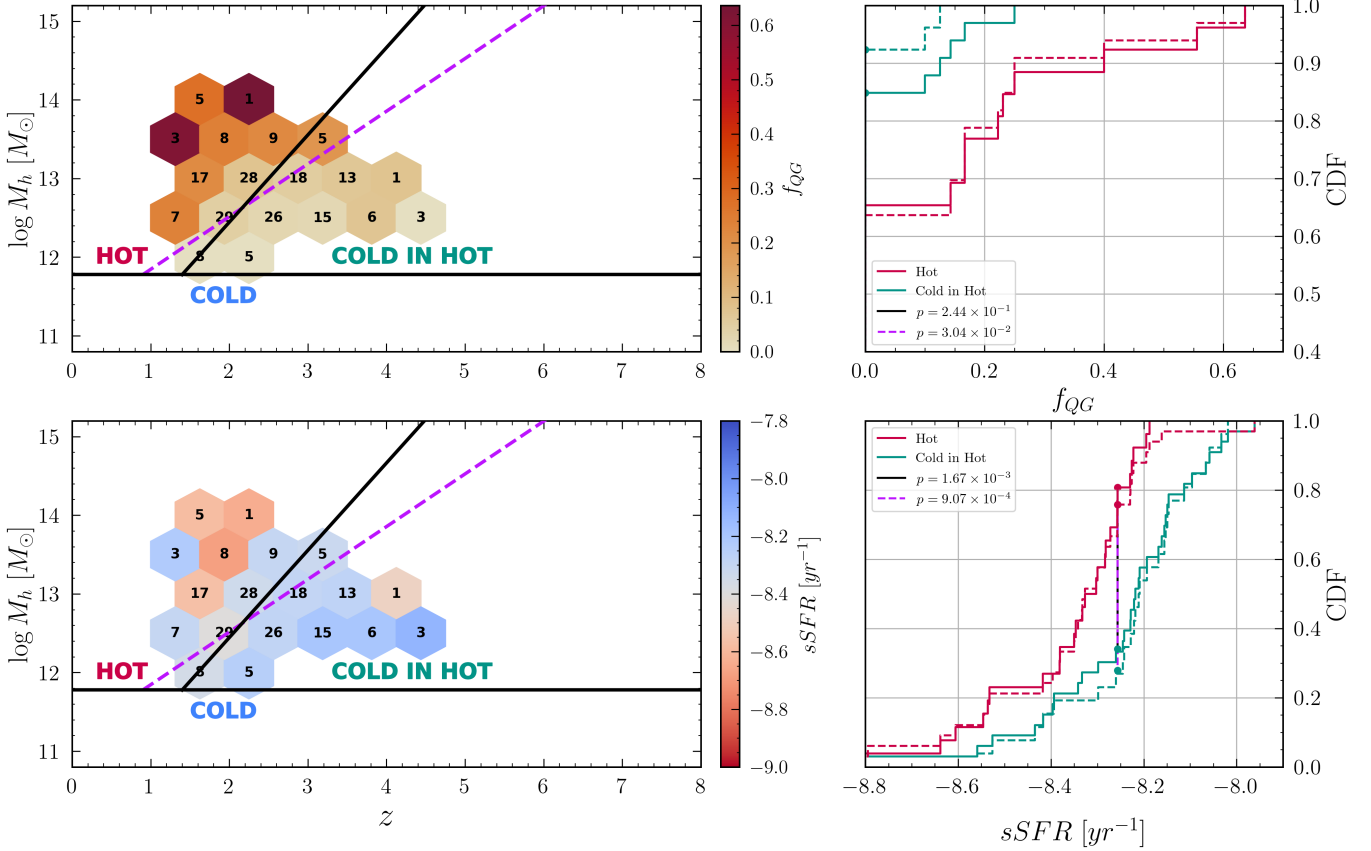


Figure 8. Hexbin plot of the galaxy systems distribution from Figure 5. Dividing lines corresponds to the definition of the halo accretion modes predicted by A. Dekel & Y. Birnboim (2006) (black solid line) and E. Daddi et al. (2022b) (purple dashed line). *Top panel:* Hexbin plot of halo mass with respect to quiescent galaxies fraction. *Bottom panel:* Hexbin plot of halo mass with respect to their $sSFR$. Each bin represents the median of the overdensities inside the bin. The number represents the total number of overdensities within the bin. The right panel show the Kolmogorov-Smirnov (KS) test results for each parameter distribution on different cold stream transition definitions limited for system at $2 < z < 2.5$.

Table 1. Kendall Rank Correlation Coefficient Test Results Presented in τ Statistics for Quiescent Fraction (f_Q) and Specific Star Formation Rate ($sSFR$) Relative to Local Density

Parameters	Redshift	Correlation Coeff. (τ)	p -value
f_{QG}	$1.5 < z < 2$	0.588	0.047
	$2 < z < 3$	0.244	0.467
	$3 < z < 5$	-0.067	0.639
M_*	$1.5 < z < 2$	0.685	0.015
	$2 < z < 3$	0.345	0.223
	$3 < z < 5$	0.127	0.601
$sSFR$	$1.5 < z < 2$	-0.612	0.029
	$2 < z < 3$	-0.200	0.484
	$3 < z < 5$	0.378	0.216

infalling gas is not shock-heated because the cooling

timescale is shorter than the dynamical timescale. This allows cold gas to efficiently reach the central galaxy. In more massive halos, however, infalling gas is subject to shock-heating to the virial temperature, forming a stable hot halo that suppresses cold inflows and limits the fuel available for star formation.

Narrow streams of cold gas may nevertheless penetrate the hot circumgalactic medium (CGM), continuing to supply star-forming fuel to the central galaxy. This transition is described by the cold-stream model of galaxy formation (also N. Mandelker et al. 2020). Cold streams can penetrate hot halos for systems with $M_h < M_{\text{stream}}(z)$, where $M_{\text{stream}}(z)$ defines the redshift-dependent boundary of the cold-stream regime. Conversely, in halos with $M_h > M_{\text{stream}}(z)$, cold streams are expected to be shock-heated nevertheless before reaching the central regions, effectively quenching star formation.

Based on this theoretical framework, the star-forming properties of galaxies in groups and protoclusters are

expected to show dependency on their host halo mass as well as redshift. To examine this in our overdensity samples, we construct a hexagonally binned plot (Figure 8). First, to qualitatively explore any trends, we color-code each hexagonal point by the quenched fraction (top) and specific star formation rate (sSFR; bottom) of galaxy systems as functions of halo mass and redshift. We overlaid the theoretical boundaries separating the cold, hot, and transitional (cold-in-hot) accretion regimes, as defined by [A. Dekel & Y. Birnboim \(2006\)](#) and [E. Daddi et al. \(2022b\)](#).

Most overdensities identified in our study lie above the critical shock-heating mass. Even so, both quenched fraction and sSFR show clear dependencies on halo mass and redshift, consistent with the gas-accretion models of [A. Dekel & Y. Birnboim \(2006\)](#) and [E. Daddi et al. \(2022b\)](#). The gradient traced by the hexbin colors is inclined in the same sense predicted by these models. Along this transition, quiescent fraction increases while sSFR decreases toward lower redshift. This behavior is naturally expected from the following sequence: once a halo becomes fully shock-heated, cold gas accretion is suppressed, halting the inflow of fresh gas needed to sustain star formation. As a result, star formation rates gradually decline, increasing the quiescent fraction and decreasing sSFR of the member galaxies therein, as observed in our samples.

We quantitatively assess differences in galaxy properties between those in the hot accretion region and those in the cold-in-hot region using a Kolmogorov–Smirnov (K–S) test as shown in the right panel of Figure 8. To minimize redshift-driven variation and isolate halo-mass dependence, we restrict the analysis to overdensities at $2.0 < z < 2.5$, which provides sufficient samples in both regimes. The K–S test reveals statistically significant differences ($p < 0.05$) between systems properties in the hot region and those in the cold-in-hot region, except for the [A. Dekel & Y. Birnboim \(2006\)](#) boundary when considering the quiescent fraction. These results are consistent with [E. Daddi et al. \(2022a\)](#), which found an improved statistical separation when using the cold-stream boundary of [E. Daddi et al. \(2022b\)](#).

We also examine how these parameters in our sample evolve with respect to the distance from the cold-stream definition (ΔM_{stream} ; Figure 9). The quiescent fraction shows a clear dependence on ΔM_{stream} : it increases as the distance grows larger, particularly for systems in the hot region. In contrast, this trend is absent in the cold-in-hot region, which presents a flattening trend, similar to the results from [E. Daddi et al. \(2022a\)](#), although with different tracers. This can happen mainly because most systems contain no quiescent galaxies, resulting

in quiescent fractions of zero. This behavior supports the cold-stream scenario, where dense cold gas can still penetrate massive halos in the transitional regime, sustaining star formation. A similarly clear trend is seen in sSFR: as ΔM_{stream} increases, the median sSFR decreases in hot-region systems, indicating more efficient star-formation suppression. Conversely, in the cold-in-hot region, sSFR increases as ΔM_{stream} becomes larger.

This result is consistent with predicted satellite galaxy behavior at high redshift from simulations. [F. van de Voort et al. \(2017\)](#), using the hydrodynamical EAGLE simulation, reported a clear dependence of gas accretion suppression on the host halo mass at $z \sim 2$: larger host halos correspond to lower gas accretion rates, even at high redshift. This aligns with quenching scenarios in which the main halo suppresses gas accretion onto infalling galaxies, effectively enhancing the efficiency of the galaxy quenching processes.

5.2. Environmental Effect at the Local Scale

Figure 7 shows the trends between galaxy parameters and their dependence on the overdensity factor, which represents the local-scale environment. Up to $z \approx 3$, all parameters show consistent behavior: the quiescent fraction and the median stellar mass increase, while sSFR decreases, with overdensity. However, Kendall’s tau value indicate that these trends are statistically significant only at $1.5 < z < 2$, as shown by the p –values below 0.05, allowing us to reject the null hypothesis that the observed correlations are random.

With caution regarding direct comparisons of overdensity values, we compare these trends with previous studies. The environmental dependence of the quiescent fraction has been reported by [G. Toni et al. \(2025\)](#) and [K. Shi et al. \(2024\)](#). [G. Toni et al. \(2025\)](#) found that quiescent fraction increases with increasing group richness (number of the galaxies within the system), which itself correlates with local density, with this trend emerging at $z < 2$. [K. Shi et al. \(2024\)](#) also found similar behavior between the quiescent fraction and the overdensity, and reported no significant environmental dependence beyond $z > 2$, consistent with our results.

For galaxy properties, our findings are generally consistent with previous work. The stellar mass increases with overdensity up to $z < 3$, consistent with [S. Taamoli et al. \(2024\)](#), [K. Shi et al. \(2024\)](#) [H. Hatamnia et al. \(2025\)](#), and [N. Chartab et al. \(2025\)](#). Similarly, [I. McConachie et al. \(2025\)](#) found that the majority ($> 75\%$) of their spectroscopically-confirmed massive quiescent galaxies at $3 < z < 5$ preferentially reside in overdensity peaks. They suggest that the mass build-up of these galaxies reflects a significant contribution from

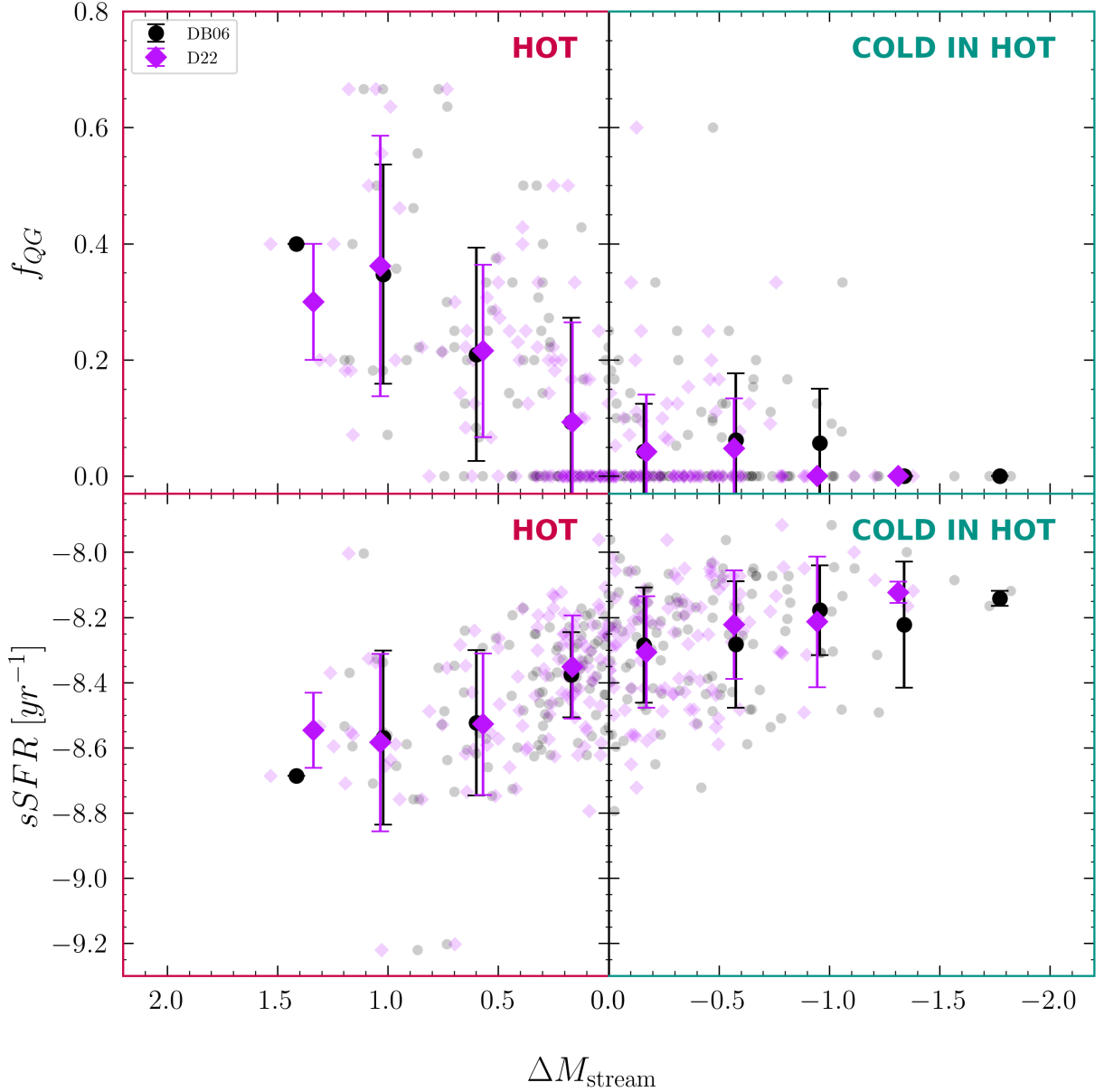


Figure 9. Quiescent fraction (top) and sSFR (bottom) with respect to the distance of halo mass to the cold-stream definition (ΔM_{stream}). The half-transparent data point corresponds to each system's properties, while the solid-colored data point and its error bar corresponds to the mean and standard deviation (scatter) of each bin. The left panel shows systems in the hot region, and the right panel shows systems in the cold-in-hot region. The DB06 data point is based on the [A. Dekel & Y. Birnboim \(2006\)](#) cold-streams definition, while D22 is based on [E. Daddi et al. \(2022b\)](#).

ex-situ star formation via major mergers. This is supported by simulation results from [F. Huško et al. \(2023\)](#), which used the GALFORM semi-analytical model with the Planck-Millennium simulation, indicating that most stellar mass of massive galaxies forms through ex-situ processes, including mergers. Observationally, merger rates also correlate with environment; for example, [T. Shibuya et al. \(2025\)](#) show that the relative major merger rate strongly depends on overdensity for galaxies at $2 < z < 5$. Similar trends have been reported in both

local and intermediate-redshift galaxy samples, indicating that local density plays an important role in shaping the galaxy stellar mass function ([B. Vulcani et al. 2012](#); [A. R. Tomczak et al. 2017](#)).

For sSFR, our results agree with previous studies ([D. Elbaz et al. 2007](#); [M. C. Cooper et al. 2008](#); [B. Darvish et al. 2016](#); [N. Chartab et al. 2020](#)), who found an anti-correlation with overdensity. However, more recent studies ([B. Lemaux et al. 2022](#); [S. Taamoli et al. 2024](#); [K. Shi et al. 2024](#); [H. Hatamnia et al. 2025](#)) report a rever-

sal in this relation, with sSFR positively correlating with overdensity, although the transition epoch remains uncertain. K. Shi et al. (2024) note that discrepancies may arise from the mass-completeness limit in earlier studies, which can cause mass quenching to dominate observed trends. We too here observe the reversal trends in our study from the plot in Figure 7 and Kendall’s statistics. However, our limited sample size, particularly at high redshift, reduces the statistical significance of these results. In addition, increasing photometric redshift uncertainties at higher redshifts may further contribute to this effect. This highlights the need for future studies extending to lower stellar masses to confirm whether these potential reversal trends persist.

Combining these results, we conclude that galaxy properties correlate with local density up to $z < 2$. Galaxies in higher-density environments tend to be more massive, with a large fraction either undergoing or having already experienced quenching. This suggests that dense environments either promote rapid mass assembly or accelerate quenching processes.

Such behavior is consistent with the overconsumption scenario (S. L. McGee et al. 2014; M. L. Balogh et al. 2016), in which satellite galaxies in dense regions quench as a result of suppressed cold-gas accretion combined with outflow-driven gas depletion after entering a massive halo, a process often referred to as starvation or strangulation. This mechanism is expected to be more efficient for massive galaxies, in agreement with our findings on the dependence of the quiescent fraction and sSFR on both halo mass and local density. Furthermore, F. van de Voort et al. (2017) demonstrated that gas accretion rates onto galaxies decrease with increasing local density, consistent with our results that galaxies residing in denser environments experience reduced gas supply.

6. CONCLUSION

In this paper, we utilized the 20 deepest fields in the Bias-free Extragalactic Analysis for Cosmic Origins with NIRCam (BEACON) survey to systematically search for galaxy overdensities at $1.5 < z < 7$, an unprecedented number of independent fields observed to JWST depths. From the identified overdensities and quantified local densities, we investigate the effect of environment on galaxy properties, especially their quenching mechanism. We summarize our findings as follows:

1. We have identified 207 significant ($> 4\sigma$) galaxy overdensity at $1.5 < z < 5$ using weighted adaptive kernel density estimation in 20 independent NIRCam fields from BEACON, with peak overdensity factor (δ) ranging from 3 to 30. Using stellar-to-halo mass relation (SHMR), we determine the halo

mass of each system, obtaining systems with mass ranging from 1.2×10^{12} to $1.2 \times 10^{14} M_{\odot}$

2. By comparing total halo masses to star-forming properties, we find evidence consistent with the predictions of the cold-stream model of galaxy formation. We identify two distinct quenching regimes: a “hot” regime where massive halos efficiently suppress star formation at $z \sim 2$, and a “cold-in-hot” regime at higher redshifts where star formation persists despite high halo mass.
3. We observe significant correlations between local density and galaxy properties at $z < 2$, where higher densities correspond to increased quiescent fractions, higher median stellar masses, and suppressed specific star formation rates (sSFR). These trends weaken significantly at $z > 2$, indicating that environmental quenching mechanisms only become dominant as the universe matures.
4. Galaxy overdensity properties show dependence on the vertical distance of halo mass from the cold-stream mass definition, particularly for systems located in the hot region.
5. Our findings are consistent with the overconsumption scenario, where galaxy quenching in overdense regions is driven by outflow processes combined with the suppression of cold gas accretion.

Our results are broadly consistent with previous studies and offer additional observational constraints on galaxy evolution scenarios such as cold-stream accretion and overconsumption models. Spectroscopic follow-up will be required to confirm the overdense structures identified in this work and to robustly assess their physical nature, to further test the conclusions presented here. Future studies combining pure-parallel observations with the high spatial resolution of JWST will also enable detailed investigations of the connection between galaxy morphology and environment, as well as the occurrence of rare populations, including clumpy galaxies and dusty star-forming galaxies (DSFGs) in various environments.

ACKNOWLEDGMENTS

The kernel density estimation calculations were carried out on the Multi-wavelength Data Analysis System operated by the Astronomy Data Center (ADC), National Astronomical Observatory of Japan. Support for JWST program 3990 was provided by NASA through the Space Telescope Science Institute, which is operated by the Association of Universities for Research in Astronomy, Inc., under NASA contract NAS 5-03127. RAS, TK, NSH, and KT acknowledge financial support from the

Japanese Government (Ministry of Education, Culture, Sports, Science and Technology; MEXT), the Graduate Program on Physics for the Universe (GP-PU) at Tohoku University, JSPS KAKENHI Grant Numbers 24H00002 (Specially Promoted Research by T. Kodama et al.), 22K21349 (International Leading Research by S. Miyazaki et al.), and JSPS Core-to-Core Program (JPJSCCA20210003; M. Yoshida et al.). MJH is supported by the Swedish Research Council (Vetenskapsrådet) and is a Fellow of the Knut and Alice Wallenberg Foundation. All of the data presented in this paper were obtained from the Mikulski Archive for Space

Telescopes (MAST) at the Space Telescope Science Institute. The specific observations analyzed can be accessed via [10.17909/swvp-0160](https://doi.org/10.17909/swvp-0160).

Facilities: James Webb Space Telescope (JWST)

Software: ASTROPY ([Astropy Collaboration et al. 2013, 2018, 2022](#)) EAZY-PY ([G. B. Brammer et al. 2008](#)), CIGALE ([M. Boquien et al. 2019](#)), SExtractor ([E. Bertin & S. Arnouts 1996](#)), UNIVERSE MACHINE ([P. Behroozi et al. 2019](#))

APPENDIX

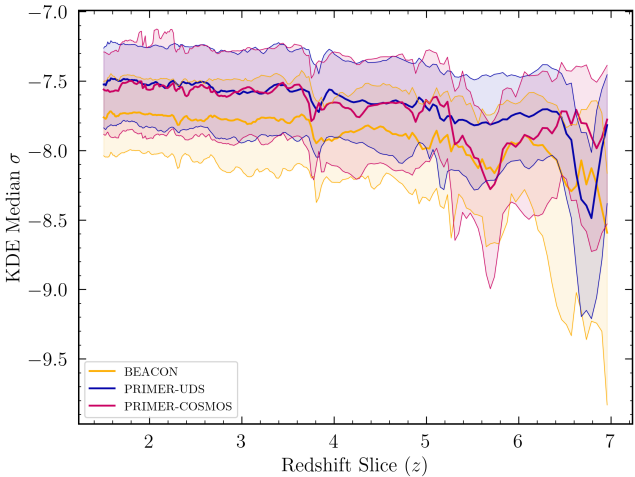


Figure 10. Comparison of measured median of surface density by kernel density estimation from the BEACON, PRIMER-UDS, and PRIMER-COSMOS fields. Each field is represented by different colors, where the solid lines represent the median of the distribution on each redshift and the shaded region represents the range given by the 16th and 84th percentiles.

A. VALIDITY OF THE ABSOLUTE OVERDENSITY FACTOR

The surface density maps derived from the adaptive kernel density estimation are presented in arbitrary, non-normalized units by definition. As described in Section 4.1, the overdensity factor at each position is calculated by normalizing the local surface density by the median surface density in each redshift slice. However, this normalization is field-dependent, meaning that the median value varies between the BEACON fields. This variation arises from the relatively small footprint of

each field, which could be susceptible to cosmic variance in some cases. Consequently, the median surface density of our fields may not represent a typical field environment. To mitigate this, we have adopted a single median value computed across all BEACON fields within each redshift slice.

To further assess this issue, we simulated our observation and analysis procedure on other JWST fields with comparable depth, namely, the PRIMER survey (JWST-GO-1837; [J. S. Dunlop et al. 2021](#)) in the UDS and COSMOS regions. Specifically, we randomly placed a NIRCam mosaic footprint within each PRIMER field and extracted galaxies located inside the footprint. This process was repeated 50 times per field to generate independent realizations. For each realization, we performed photometric redshift fitting using the same configuration described in Section 2.2, and constructed overdensity maps following the procedure in Section 3. Through this simulation, we aim to evaluate how well a small NIRCam footprint can recover the true large-scale overdensity pattern and to determine the reliability of using such a limited field to represent the actual density contrast.

In Figure 10, we show the measured median value of the KDE surface density for 20 BEACON fields, 50 realizations from PRIMER-UDS, and 50 realizations from PRIMER-COSMOS across redshift slices, along with their 68% percentile range. The measured medians of surface density are consistent throughout the fields, while our BEACON dataset shows a slightly smaller value, which is likely caused by the small field of view of each field. For our final catalog and the following analysis, we calibrate the estimated overdensity factor to the median of these three surveys.

REFERENCES

Abadi, M. G., Moore, B., & Bower, R. G. 1999, *Monthly Notices of the Royal Astronomical Society*, 308, 947

Abramson, I. S. 1982, *The annals of Statistics*, 1217

ACTDES-HSC Collaboration, Aguena, M., Aiola, S., et al. 2025, arXiv e-prints, arXiv:2507.21459, doi: [10.48550/arXiv.2507.21459](https://doi.org/10.48550/arXiv.2507.21459)

Adachi, K., Kodama, T., Pérez-Martínez, J. M., Suzuki, T. L., & Onodera, M. 2025, arXiv preprint arXiv:2506.01088

Adam, R., Vannier, M., Maurogordato, S., et al. 2019, *Astronomy & Astrophysics*, 627, A23

Arribas, S., Perna, M., Rodríguez Del Pino, B., et al. 2024, *A&A*, 688, A146, doi: [10.1051/0004-6361/202348824](https://doi.org/10.1051/0004-6361/202348824)

Astropy Collaboration, Robitaille, T. P., Tollerud, E. J., et al. 2013, *A&A*, 558, A33, doi: [10.1051/0004-6361/201322068](https://doi.org/10.1051/0004-6361/201322068)

Astropy Collaboration, Price-Whelan, A. M., Sipőcz, B. M., et al. 2018, *AJ*, 156, 123, doi: [10.3847/1538-3881/aabc4f](https://doi.org/10.3847/1538-3881/aabc4f)

Astropy Collaboration, Price-Whelan, A. M., Lim, P. L., et al. 2022, *ApJ*, 935, 167, doi: [10.3847/1538-4357/ac7c74](https://doi.org/10.3847/1538-4357/ac7c74)

Balestra, I., Mainieri, V., Popesso, P., et al. 2010, *A&A*, 512, A12, doi: [10.1051/0004-6361/200913626](https://doi.org/10.1051/0004-6361/200913626)

Balogh, M. L., McGee, S. L., Mok, A., et al. 2016, *Monthly Notices of the Royal Astronomical Society*, 456, 4364

Behroozi, P., Wechsler, R. H., Hearn, A. P., & Conroy, C. 2019, *MNRAS*, 488, 3143, doi: [10.1093/mnras/stz1182](https://doi.org/10.1093/mnras/stz1182)

Behroozi, P. S., Wechsler, R. H., & Conroy, C. 2013, *ApJ*, 770, 57, doi: [10.1088/0004-637X/770/1/57](https://doi.org/10.1088/0004-637X/770/1/57)

Bellstedt, S., & Robotham, A. S. 2025, *Monthly Notices of the Royal Astronomical Society*, 540, 2703

Bertin, E., & Arnouts, S. 1996, *A&AS*, 117, 393, doi: [10.1051/aas:1996164](https://doi.org/10.1051/aas:1996164)

Bielby, R. M., Gonzalez-Perez, V., McCracken, H. J., et al. 2014, *A&A*, 568, A24, doi: [10.1051/0004-6361/201322814](https://doi.org/10.1051/0004-6361/201322814)

Bocquet, S., Dietrich, J. P., Schrabbback, T., et al. 2019, *ApJ*, 878, 55, doi: [10.3847/1538-4357/ab1f10](https://doi.org/10.3847/1538-4357/ab1f10)

Boquien, M., Burgarella, D., Roehlly, Y., et al. 2019, *A&A*, 622, A103, doi: [10.1051/0004-6361/201834156](https://doi.org/10.1051/0004-6361/201834156)

Bradley, L., Trenti, M., Oesch, P., et al. 2012, *The Astrophysical Journal*, 760, 108

Brammer, G. B., van Dokkum, P. G., & Coppi, P. 2008, *ApJ*, 686, 1503, doi: [10.1086/591786](https://doi.org/10.1086/591786)

Brammer, G. B., van Dokkum, P. G., Franx, M., et al. 2012, *ApJS*, 200, 13, doi: [10.1088/0067-0049/200/2/13](https://doi.org/10.1088/0067-0049/200/2/13)

Brinch, M., Greve, T. R., Weaver, J. R., et al. 2023, *ApJ*, 943, 153, doi: [10.3847/1538-4357/ac9d96](https://doi.org/10.3847/1538-4357/ac9d96)

Bruzual, G., & Charlot, S. 2003, *MNRAS*, 344, 1000, doi: [10.1046/j.1365-8711.2003.06897.x](https://doi.org/10.1046/j.1365-8711.2003.06897.x)

Bunker, A. J., Cameron, A. J., Curtis-Lake, E., et al. 2024, *Astronomy & Astrophysics*, 690, A288

Butcher, H., & Oemler Jr, A. 1978, *Astrophysical Journal*, Part 1, vol. 219, Jan. 1, 1978, p. 18-30., 219, 18

Calzetti, D., Armus, L., Bohlin, R. C., et al. 2000, *ApJ*, 533, 682, doi: [10.1086/308692](https://doi.org/10.1086/308692)

Capak, P. L., Riechers, D., Scoville, N. Z., et al. 2011, *Nature*, 470, 233, doi: [10.1038/nature09681](https://doi.org/10.1038/nature09681)

Cardelli, J. A., Clayton, G. C., & Mathis, J. S. 1989, *Astrophysical Journal*, Part 1 (ISSN 0004-637X), vol. 345, Oct. 1, 1989, p. 245-256., 345, 245

Carnall, A., McLeod, D., McLure, R., et al. 2023, *Monthly Notices of the Royal Astronomical Society*, 520, 3974

Casey, C. M., Cooray, A., Capak, P., et al. 2015, *ApJL*, 808, L33, doi: [10.1088/2041-8205/808/2/L33](https://doi.org/10.1088/2041-8205/808/2/L33)

Chabrier, G. 2003, *PASP*, 115, 763, doi: [10.1086/376392](https://doi.org/10.1086/376392)

Chanchaiworawit, K., Guzmán, R., Salvador-Solé, E., et al. 2019, *ApJ*, 877, 51, doi: [10.3847/1538-4357/ab1a34](https://doi.org/10.3847/1538-4357/ab1a34)

Chartab, N., Mobasher, B., Darvish, B., et al. 2020, *ApJ*, 890, 7, doi: [10.3847/1538-4357/ab61fd](https://doi.org/10.3847/1538-4357/ab61fd)

Chartab, N., Mobasher, B., Shapley, A. E., et al. 2021, *The Astrophysical Journal*, 908, 120

Chartab, N., Newman, A. B., Rudie, G. C., et al. 2025, *The Astrophysical Journal*, 994, 106

Chen, S. X. 1999, *Computational Statistics & Data Analysis*, 31, 131

Chen, S. X. 2000, *Annals of the institute of statistical mathematics*, 52, 471

Cheng, M.-Y. 1997, *Journal of the Royal Statistical Society: Series B (Statistical Methodology)*, 59, 191

Chiang, Y.-K., Overzier, R., & Gebhardt, K. 2013, *ApJ*, 779, 127, doi: [10.1088/0004-637X/779/2/127](https://doi.org/10.1088/0004-637X/779/2/127)

Chiang, Y.-K., Overzier, R., & Gebhardt, K. 2013, *The Astrophysical Journal*, 779, 127

Cole, S., Lacey, C. G., Baugh, C. M., & Frenk, C. S. 2000, *Monthly Notices of the Royal Astronomical Society*, 319, 168

Conroy, C., White, M., & Gunn, J. E. 2010, *ApJ*, 708, 58, doi: [10.1088/0004-637X/708/1/58](https://doi.org/10.1088/0004-637X/708/1/58)

Cooper, M. C., Newman, J. A., Weiner, B. J., et al. 2008, *Monthly Notices of the Royal Astronomical Society*, 383, 1058

Cowling, A., & Hall, P. 1996, *Journal of the Royal Statistical Society Series B: Statistical Methodology*, 58, 551

Cucciati, O., Zamorani, G., Lemaux, B. C., et al. 2014, *A&A*, 570, A16, doi: [10.1051/0004-6361/201423811](https://doi.org/10.1051/0004-6361/201423811)

Curran, P. A. 2014, arXiv preprint arXiv:1411.3816

Curtis-Lake, E., Cameron, A. J., Bunker, A. J., et al. 2025, arXiv preprint arXiv:2510.01033

Daddi, E., Rich, R. M., Valentino, F., et al. 2022a, *The Astrophysical Journal Letters*, 926, L21

Daddi, E., Delvecchio, I., Dimauro, P., et al. 2022b, *Astronomy & Astrophysics*, 661, L7

Daikuhara, K., Kodama, T., Kusakabe, H., et al. 2025, *Monthly Notices of the Royal Astronomical Society*, 544, 2365

Darvish, B., Mobasher, B., Sobral, D., et al. 2016, *The Astrophysical Journal*, 825, 113

Darvish, B., Mobasher, B., Sobral, D., Scoville, N., & Aragon-Calvo, M. 2015, *ApJ*, 805, 121, doi: [10.1088/0004-637X/805/2/121](https://doi.org/10.1088/0004-637X/805/2/121)

Davis, A. J., D'Aloisio, A., & Natarajan, P. 2011, *Monthly Notices of the Royal Astronomical Society*, 416, 242

Dekel, A., & Birnboim, Y. 2006, *MNRAS*, 368, 2, doi: [10.1111/j.1365-2966.2006.10145.x](https://doi.org/10.1111/j.1365-2966.2006.10145.x)

Dekel, A., Birnboim, Y., Engel, G., et al. 2009, *Nature*, 457, 451

Di Mascolo, L., Saro, A., Mroczkowski, T., et al. 2023, *Nature*, 615, 809, doi: [10.1038/s41586-023-05761-x](https://doi.org/10.1038/s41586-023-05761-x)

Diggle, P. 1985, *Journal of the Royal Statistical Society: Series C (Applied Statistics)*, 34, 138

Dressler, A. 1980, *Astrophysical Journal*, Part 1, vol. 236, Mar. 1, 1980, p. 351-365., 236, 351

Dunlop, J. S., Abraham, R. G., Ashby, M. L. N., et al. 2021, PRIMER: Public Release IMaging for Extragalactic Research., JWST Proposal. Cycle 1, ID. #1837

Durkalec, A., Le Fèvre, O., Pollo, A., et al. 2018, *A&A*, 612, A42, doi: [10.1051/0004-6361/201730734](https://doi.org/10.1051/0004-6361/201730734)

D'Eugenio, F., Cameron, A. J., Scholtz, J., et al. 2025, *The Astrophysical Journal Supplement Series*, 277, 4

Edward, A. H., Balogh, M. L., Bahe, Y. M., et al. 2024, *Monthly Notices of the Royal Astronomical Society*, 527, 8598

Elbaz, D., Daddi, E., Le Borgne, D., et al. 2007, *Astronomy & Astrophysics*, 468, 33

Ferland, G., Korista, K., Verner, D., et al. 1998, *Publications of the Astronomical Society of the Pacific*, 110, 761

Ferland, G. J., Porter, R., Van Hoof, P., et al. 2013, *Revista mexicana de astronomía y astrofísica*, 49, 137

Finkelstein, S. L., Bagley, M. B., Ferguson, H. C., et al. 2023, *The Astrophysical journal letters*, 946, L13

Fukugita, M., Shimasaku, K., & Ichikawa, T. 1995, *Publications of the Astronomical Society of the Pacific*, 107, 945

Garilli, B., McLure, R., Pentericci, L., et al. 2021, *A&A*, 647, A150, doi: [10.1051/0004-6361/202040059](https://doi.org/10.1051/0004-6361/202040059)

Grogin, N. A., Kocevski, D. D., Faber, S. M., et al. 2011, *ApJS*, 197, 35, doi: [10.1088/0067-0049/197/2/35](https://doi.org/10.1088/0067-0049/197/2/35)

Gunn, J. E., & Gott III, J. R. 1972, *Astrophysical Journal*, vol. 176, p. 1, 176, 1

Hall, P. 1982, *Biometrika*, 69, 383

Harikane, Y., Ouchi, M., Ono, Y., et al. 2018, *PASJ*, 70, S11, doi: [10.1093/pasj/psx097](https://doi.org/10.1093/pasj/psx097)

Harikane, Y., Ouchi, M., Ono, Y., et al. 2019, *ApJ*, 883, 142, doi: [10.3847/1538-4357/ab2cd5](https://doi.org/10.3847/1538-4357/ab2cd5)

Hatamnia, H., Mobasher, B., Taamoli, S., et al. 2025, arXiv preprint arXiv:2511.10727

Helton, J. M., Sun, F., Woodrum, C., et al. 2024, *ApJ*, 962, 124, doi: [10.3847/1538-4357/ad0da7](https://doi.org/10.3847/1538-4357/ad0da7)

Huško, F., Lacey, C. G., & Baugh, C. M. 2023, *Monthly Notices of the Royal Astronomical Society*, 518, 5323

Ilbert, O., McCracken, H. J., Le Fèvre, O., et al. 2013, *Astronomy & Astrophysics*, 556, A55

Inoue, A. K. 2011, *Monthly Notices of the Royal Astronomical Society*, 415, 2920

Ito, K., Tanaka, M., Valentino, F., et al. 2023, *The Astrophysical journal letters*, 945, L9

Jespersen, C. K., Carnall, A. C., & Lovell, C. C. 2025, *ApJL*, 988, L19, doi: [10.3847/2041-8213/adeb7c](https://doi.org/10.3847/2041-8213/adeb7c)

Jones, M. C. 1993, *Statistics and computing*, 3, 135

Kendall, M. G. 1938, *Biometrika*, 30, 81

Khostovan, A. A., Kartaltepe, J. S., Salvato, M., et al. 2025, arXiv e-prints, arXiv:2503.00120, doi: [10.48550/arXiv.2503.00120](https://doi.org/10.48550/arXiv.2503.00120)

Koekemoer, A. M., Faber, S. M., Ferguson, H. C., et al. 2011, *ApJS*, 197, 36, doi: [10.1088/0067-0049/197/2/36](https://doi.org/10.1088/0067-0049/197/2/36)

Koyama, Y., Polletta, M. d. C., Tanaka, I., et al. 2021, *MNRAS*, 503, L1, doi: [10.1093/mnrasl/slab013](https://doi.org/10.1093/mnrasl/slab013)

Laporte, N., Zitrin, A., Dole, H., et al. 2022, *A&A*, 667, L3, doi: [10.1051/0004-6361/202244719](https://doi.org/10.1051/0004-6361/202244719)

Larson, R. B., Tinsley, B. M., & Caldwell, C. N. 1980, *Astrophysical Journal*, Part 1, vol. 237, May 1, 1980, p. 692-707. Research supported by the Alfred P. Sloan Foundation, 237, 692

Lemaux, B., Cucciati, O., Le Fèvre, O., et al. 2022, *Astronomy & Astrophysics*, 662, A33

Li, Q., Yang, X., Liu, C., et al. 2022, *ApJ*, 933, 9, doi: [10.3847/1538-4357/ac6e69](https://doi.org/10.3847/1538-4357/ac6e69)

Liu, Z., Kodama, T., Lemaux, B. C., et al. 2025, *ApJ*, 995, 81, doi: [10.3847/1538-4357/ae0c02](https://doi.org/10.3847/1538-4357/ae0c02)

Madau, P., & Dickinson, M. 2014, *Annual Review of Astronomy and Astrophysics*, 52, 415

Mandelker, N., Nagai, D., Aung, H., et al. 2020, *Monthly Notices of the Royal Astronomical Society*, 494, 2641

Marron, J. S., & Ruppert, D. 1994, *Journal of the Royal Statistical Society: Series B (Methodological)*, 56, 653

Mason, C. A., Trenti, M., & Treu, T. 2023, *MNRAS*, 521, 497, doi: [10.1093/mnras/stad035](https://doi.org/10.1093/mnras/stad035)

McConachie, I., Wilson, G., Forrest, B., et al. 2022, *The Astrophysical Journal*, 926, 37

McConachie, I., de Graaff, A., Maseda, M. V., et al. 2025, arXiv preprint arXiv:2510.25024

McGee, S. L., Bower, R. G., & Balogh, M. L. 2014, *Monthly Notices of the Royal Astronomical Society: Letters*, 442, L105

Meneux, B., Guzzo, L., Garilli, B., et al. 2008, *A&A*, 478, 299, doi: [10.1051/0004-6361:20078182](https://doi.org/10.1051/0004-6361:20078182)

Miller, T. B., Chapman, S. C., Aravena, M., et al. 2018, *Nature*, 556, 469, doi: [10.1038/s41586-018-0025-2](https://doi.org/10.1038/s41586-018-0025-2)

Moore, B., Katz, N., Lake, G., Dressler, A., & Oemler, A. 1996, *nature*, 379, 613

Moore, B., Lake, G., & Katz, N. 1998, *The Astrophysical Journal*, 495, 139

Morishita, T., Trenti, M., Stiavelli, M., et al. 2018, *The Astrophysical Journal*, 867, 150

Morishita, T., Stiavelli, M., Trenti, M., et al. 2020, *The Astrophysical Journal*, 904, 50

Morishita, T., Roberts-Borsani, G., Treu, T., et al. 2023, *ApJL*, 947, L24, doi: [10.3847/2041-8213/acb99e](https://doi.org/10.3847/2041-8213/acb99e)

Morishita, T., Liu, Z., Stiavelli, M., et al. 2025a, *ApJ*, 982, 153, doi: [10.3847/1538-4357/adb30f](https://doi.org/10.3847/1538-4357/adb30f)

Morishita, T., Mason, C. A., Kreilgaard, K. C., et al. 2025b, *ApJ*, 983, 152, doi: [10.3847/1538-4357/adbbdc](https://doi.org/10.3847/1538-4357/adbbdc)

Morishita, T., Stiavelli, M., Vanzella, E., et al. 2025c, *ApJ*, 985, 83, doi: [10.3847/1538-4357/adc4c3](https://doi.org/10.3847/1538-4357/adc4c3)

Muldrew, S. I., Hatch, N. A., & Cooke, E. A. 2015, *Monthly Notices of the Royal Astronomical Society*, 452, 2528

Müller, H.-G. 1991, *Biometrika*, 78, 521

Muzzin, A., Marchesini, D., Stefanon, M., et al. 2013, *The Astrophysical Journal*, 777, 18

Naufal, A., Koyama, Y., D'Eugenio, C., et al. 2024, *The Astrophysical Journal*, 977, 58

Newman, A. B., Ellis, R. S., Andreon, S., et al. 2014, *The Astrophysical Journal*, 788, 51

Oke, J. B., & Gunn, J. E. 1983, *ApJ*, 266, 713, doi: [10.1086/160817](https://doi.org/10.1086/160817)

Oteo, I., Ivison, R. J., Dunne, L., et al. 2018, *ApJ*, 856, 72, doi: [10.3847/1538-4357/aa1f1](https://doi.org/10.3847/1538-4357/aa1f1)

Overzier, R. A. 2016, *A&A Rv*, 24, 14, doi: [10.1007/s00159-016-0100-3](https://doi.org/10.1007/s00159-016-0100-3)

Pérez-Martínez, J. M., Kodama, T., Koyama, Y., et al. 2024, *Monthly Notices of the Royal Astronomical Society*, 527, 10221

Pérez-Martínez, J. M., Dannerbauer, H., Emonts, B. H. C., et al. 2025, *A&A*, 696, A236, doi: [10.1051/0004-6361/202450785](https://doi.org/10.1051/0004-6361/202450785)

Polletta, M., Soucail, G., Dole, H., et al. 2021, *A&A*, 654, A121, doi: [10.1051/0004-6361/202140612](https://doi.org/10.1051/0004-6361/202140612)

Pozzetti, L., Bolzonella, M., Zucca, E., et al. 2010, *A&A*, 523, A13, doi: [10.1051/0004-6361/200913020](https://doi.org/10.1051/0004-6361/200913020)

Qiu, Y., Wyithe, J. S. B., Oesch, P. A., et al. 2018, *MNRAS*, 481, 4885, doi: [10.1093/mnras/sty2633](https://doi.org/10.1093/mnras/sty2633)

Schlafly, E. F., & Finkbeiner, D. P. 2011, *ApJ*, 737, 103, doi: [10.1088/0004-637X/737/2/103](https://doi.org/10.1088/0004-637X/737/2/103)

Schlegel, D. J., Finkbeiner, D. P., & Davis, M. 1998, *ApJ*, 500, 525, doi: [10.1086/305772](https://doi.org/10.1086/305772)

Schmidt, K. B., Treu, T., Trenti, M., et al. 2014, *The Astrophysical Journal*, 786, 57

Schuster, E. F. 1985, *Communications in Statistics-Theory and methods*, 14, 1123

Shi, K., Malavasi, N., Toshikawa, J., & Zheng, X. 2024, *ApJ*, 961, 39, doi: [10.3847/1538-4357/ad11d7](https://doi.org/10.3847/1538-4357/ad11d7)

Shi, K., Malavasi, N., Toshikawa, J., & Zheng, X. 2024, *The Astrophysical Journal*, 961, 39

Shibuya, T., Ito, Y., Asai, K., et al. 2025, *Publications of the Astronomical Society of Japan*, 77, 21

Shimakawa, R., Kodama, T., Tadaki, K.-i., et al. 2015, *Monthly Notices of the Royal Astronomical Society*, 448, 666

Shimakawa, R., Kodama, T., Hayashi, M., et al. 2017, *Monthly Notices of the Royal Astronomical Society: Letters*, 468, L21

Shuntov, M., McCracken, H. J., Gavazzi, R., et al. 2022, *A&A*, 664, A61, doi: [10.1051/0004-6361/202243136](https://doi.org/10.1051/0004-6361/202243136)

Shuntov, M., Ilbert, O., Toft, S., et al. 2025, *A&A*, 695, A20, doi: [10.1051/0004-6361/202452570](https://doi.org/10.1051/0004-6361/202452570)

Sillassen, N. B., Jin, S., Magdis, G. E., et al. 2024, *Astronomy & Astrophysics*, 690, A55

Silverman, B. W. 2018, *Density estimation for statistics and data analysis* (Routledge)

Skelton, R. E., Whitaker, K. E., Momcheva, I. G., et al. 2014, *ApJS*, 214, 24, doi: [10.1088/0067-0049/214/2/24](https://doi.org/10.1088/0067-0049/214/2/24)

Springel, V., White, S. D., Jenkins, A., et al. 2005, *nature*, 435, 629

Sun, F., Egami, E., Pirzkal, N., et al. 2023, *ApJ*, 953, 53, doi: [10.3847/1538-4357/acd53c](https://doi.org/10.3847/1538-4357/acd53c)

Taamoli, S., Mobasher, B., Chartab, N., et al. 2024, *ApJ*, 966, 18, doi: [10.3847/1538-4357/ad32c5](https://doi.org/10.3847/1538-4357/ad32c5)

Taamoli, S., Nezhad, N., Mobasher, B., et al. 2024, *The Astrophysical Journal*, 977, 263

Tarrío, P., Melin, J.-B., & Arnaud, M. 2019, *A&A*, 626, A7, doi: [10.1051/0004-6361/201834979](https://doi.org/10.1051/0004-6361/201834979)

Tomczak, A. R., Lemaux, B. C., Lubin, L. M., et al. 2017, *Monthly Notices of the Royal Astronomical Society*, 472, 3512

Toni, G., Maturi, M., Castignani, G., et al. 2025, arXiv preprint arXiv:2509.08040

Topping, M. W., Shapley, A. E., Steidel, C. C., Naoz, S., & Primack, J. R. 2018, *The Astrophysical Journal*, 852, 134

Toshikawa, J., Kashikawa, N., Overzier, R., et al. 2014, *ApJ*, 792, 15, doi: [10.1088/0004-637X/792/1/15](https://doi.org/10.1088/0004-637X/792/1/15)

Toshikawa, J., Kashikawa, N., Overzier, R., et al. 2016, *ApJ*, 826, 114, doi: [10.3847/0004-637X/826/2/114](https://doi.org/10.3847/0004-637X/826/2/114)

Trenti, M., & Stiavelli, M. 2008, *ApJ*, 676, 767, doi: [10.1086/528674](https://doi.org/10.1086/528674)

Trenti, M., Bradley, L., Stiavelli, M., et al. 2012, *The Astrophysical Journal*, 746, 55

van de Voort, F., Bahé, Y. M., Bower, R. G., et al. 2017, *Monthly Notices of the Royal Astronomical Society*, 466, 3460

van der Wel, A., Franx, M., van Dokkum, P. G., et al. 2014, *ApJ*, 788, 28, doi: [10.1088/0004-637X/788/1/28](https://doi.org/10.1088/0004-637X/788/1/28)

Vanzella, E., Cristiani, S., Dickinson, M., et al. 2008, *A&A*, 478, 83, doi: [10.1051/0004-6361:20078332](https://doi.org/10.1051/0004-6361:20078332)

Venemans, B. P., Röttgering, H. J. A., Miley, G. K., et al. 2007, *A&A*, 461, 823, doi: [10.1051/0004-6361:20053941](https://doi.org/10.1051/0004-6361:20053941)

Vulcani, B., Poggianti, B. M., Fasano, G., et al. 2012, *Monthly Notices of the Royal Astronomical Society*, 420, 1481

Wake, D. A., Whitaker, K. E., Labbé, I., et al. 2011, *ApJ*, 728, 46, doi: [10.1088/0004-637X/728/1/46](https://doi.org/10.1088/0004-637X/728/1/46)

Wang, T., Elbaz, D., Daddi, E., et al. 2016, *ApJ*, 828, 56, doi: [10.3847/0004-637X/828/1/56](https://doi.org/10.3847/0004-637X/828/1/56)

Weaver, J., Davidzon, I., Toft, S., et al. 2023, *Astronomy & Astrophysics*, 677, A184

Whitaker, K. E., Kriek, M., van Dokkum, P. G., et al. 2012, *ApJ*, 745, 179, doi: [10.1088/0004-637X/745/2/179](https://doi.org/10.1088/0004-637X/745/2/179)

Whitaker, K. E., Franx, M., Bezanson, R., et al. 2015, *ApJL*, 811, L12, doi: [10.1088/2041-8205/811/1/L12](https://doi.org/10.1088/2041-8205/811/1/L12)

White, S. D. M., & Frenk, C. S. 1991, *ApJ*, 379, 52, doi: [10.1086/170483](https://doi.org/10.1086/170483)

Williams, C. C., Oesch, P. A., Weibel, A., et al. 2025, *The Astrophysical Journal*, 979, 140

Wilson, E. B. 1927, *Journal of the American Statistical Association*, 22, 209

Yang, X., Mo, H. J., van den Bosch, F. C., et al. 2007, *ApJ*, 671, 153, doi: [10.1086/522027](https://doi.org/10.1086/522027)

Zhang, Y., Morishita, T., Kreilgaard, K. C., et al. 2026, arXiv preprint arXiv:2601.02861